Partially coherent surface plasmon polariton vortex fields

Yahong Chen,[1,2,*] Andreas Norrman,[3] Sergey A. Ponomarenko,[4,5] and Ari T. Friberg[1]
[1]*Institute of Photonics, University of Eastern Finland, P.O. Box 111, FI-80101 Joensuu, Finland*
[2]*School of Physical Science and Technology, Soochow University, Suzhou 215006, China*
[3]*Max Planck Institute for the Science of Light, Staudtstraße 2, D-91058 Erlangen, Germany*
[4]*Department of Electrical and Computer Engineering, Dalhousie University, Halifax, Nova Scotia B3J 2X4, Canada*
[5]*Department of Physics and Atmospheric Science, Dalhousie University, Halifax, Nova Scotia B3H 4R2, Canada*

(Received 11 April 2019; published 14 November 2019)

We introduce a class of partially coherent surface plasmon polariton (SPP) fields carrying optical vortices, generated through a judicious superposition of planar SPPs with a prescribed initial phase distribution and arbitrary correlations at a metal-air interface. We explore the global degree of coherence, energy densities, energy flows, orbital and spin angular momenta, and the polarization states of such partially coherent SPP vortex (SPPV) fields in terms of their coherent mode representation. The salient physical characteristics of these SPPV fields can be widely tuned by controlling the constituent SPP correlations, tailoring such SPPV fields to desired applications in statistical nanoplasmonics.

DOI: 10.1103/PhysRevA.100.053833

I. INTRODUCTION

Vortices are ubiquitous in nature, arising in such diverse physics contexts as hydrodynamic turbulence, liquid crystals, quantum superfluids, nonlinear pattern formation in complex systems, and optics [1]. In optics, in particular, vortices emerge either as line singularities in three-dimensional (3D) optical fields [2], or as isolated point singularities in the helical wave fronts of paraxial light beams [3]. The optical fields endowed with vortices can carry orbital angular momentum (OAM), rendering them highly desirable for various applications [4].

Although the majority of vortex-carrying optical fields studied to date have been fully spatially coherent, partially coherent fields with optical vortices have also been explored [5–9]. The latter were found to possess unique features, such as coherence vortices [10–12] and coherence currents [13], absent in fully coherent vortex fields. As partially coherent fields, in general, were found superior to their fully coherent counterparts in a number of applications, including speckle-free imaging [14], correlation imaging [15], information transfer through random media [16,17], as well as microparticle trapping and manipulation [18], partially coherent vortex beams, in particular, were shown to be especially well suited to control self-focusing in nonlinear optics [19] and to implement optical communication protocols through random environments [20].

At the same time, surface electromagnetic fields in plasmonics, known as the surface plasmon polaritons (SPPs), can be endowed with near-field optical vortices as well [21,22]. Fully spatially coherent SPP fields can be furnished with vortex phases by spiral plasmonic lenses [23], metallic holograms [24], and SPP interface engineering [25]. The ensuing SPP vortex (SPPV) fields have been shown to carry OAM [26], opening the door to attractive applications, for instance, in on-chip data storage [27].

To date, however, plasmonics has mainly concerned fully coherent electromagnetic fields [28]. Only lately has there been an increasing recognition that coherence, as a central degree of freedom, can be exploited to control the fundamental properties of SPP fields themselves [29–33]. Such coherence customized SPPs are expected to serve as versatile tools which could be utilized, e.g., for plasmon continuum spectroscopy [34], subwavelength white-light imaging [35], and controlled coupling of light-emitting elements [36]. Furthermore, coherence tailored SPPs have been used for synthesizing structured surface electromagnetic fields, such as partially coherent axiconlike SPP fields [37] and SPP coherence lattice fields [38]. In this context, not only does exploring partially coherent SPP fields endowed with optical vortices present fundamental interest, but it can prove instrumental in near-field optics and surface physics applications as well.

In this article, we introduce a wide class of SPPV fields with controllable coherence, generated via judicious superpositions of arbitrarily correlated planar SPPs at a metal-air interface. We stress that all salient features of the proposed SPPVs, including their energy density, energy flow, orbital and spin angular momentum, and polarization state, can be widely tuned by adjusting the spatial coherence of the fields, thereby distinguishing the present SPPV fields from the fully spatially coherent SPP fields endowed with optical vortices that have been reported to date. The broad tunability of partially coherent SPPV field distributions may well find diverse applications, ranging from controlled nanoantenna excitation and nanoparticle manipulation to near-field data storage and optical communications in advanced nanoplasmonic devices.

*Corresponding author: yahongchen@suda.edu.cn

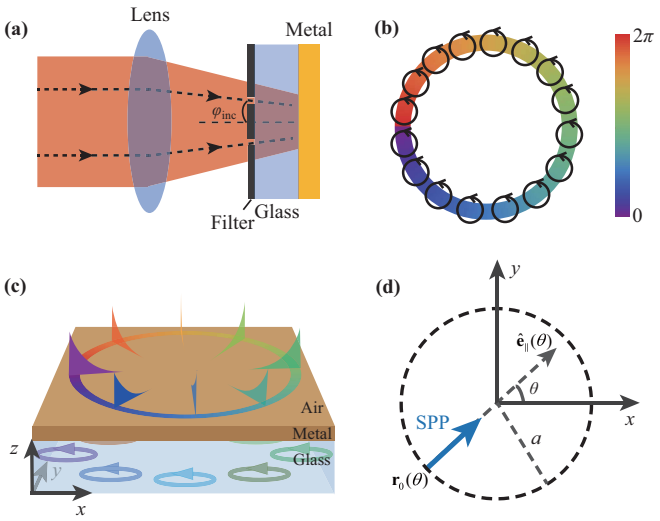

FIG. 1. Synthesis of the SPPV fields. (a) Focused circularly polarized, OAM carrying beam incident onto the circular filter, glass prism, and metal slab structure, with φ_{inc} being the angle of incidence of light selected by the filter. (b) Illustration of the polarization and phase distribution of the light on the circular ring transmitted by the filter, with $s = 1$ and $l = 1$. (c) SPPs excited on the circular ring with the desired phase distribution and propagating towards the ring center. (d) Notations related to the analysis of SPPs.

II. FIELD CHARACTERIZATION

The SPPV field geometry, akin to Kretschmann's setup [28], involves a homogeneous, isotropic, and nonmagnetic metal film deposited on a glass prism in the xy plane. The SPPV field at the metal-air interface ($z = 0$) is composed of uniformly distributed planar SPPs of a certain initial phase profile, with their origins along a circular ring of radius a, centered at the origin. The phase distribution among the SPP constituents can be introduced, e.g., with the aid of a plasmonic vortex lens [23], an optical metasurface [24], or by using a circularly polarized, OAM carrying partially spatially coherent beam as an excitation light source [39]. Prior to focusing the source beam onto the glass prism and metal film, we propose to transmit the beam through a circular spatial filter with a narrow transmission band situated in front of the prism [Fig. 1(a)]. We then obtain a ring of circularly polarized light with the phase gradient following the input beam's OAM [Fig. 1(b)]. The narrowband circular filter can also be created dynamically with the help of a spatial light modulator [40], for example. The angle of incidence φ_{inc}, controlled by the focal distance of the focusing lens, optimizes phase matching for SPP excitation [30]. The SPPs emanate from the illuminated ring with appropriate phase distributions and propagate towards the circle's center [Fig. 1(c)]. A general approach to fully coherent SPP excitation from a circular ring, but without phase matching or the vortex phases, has recently been demonstrated experimentally [41,42].

We let $\mathbf{r}_0(\theta) = -a\hat{\mathbf{e}}_{\parallel}(\theta)$ represent the excitation position of an individual SPP that propagates in the direction $\hat{\mathbf{e}}_{\parallel}(\theta) = \cos\theta\hat{\mathbf{e}}_x + \sin\theta\hat{\mathbf{e}}_y$ toward the ring center, where $0 \leqslant \theta < 2\pi$ is the azimuthal angle with respect to the x axis, and $\hat{\mathbf{e}}_x$ and $\hat{\mathbf{e}}_y$ are the Cartesian unit vectors along the x and y axes [Fig. 1(d)]. The spatial part of the electric field of an SPP in air, at point $\mathbf{r}$ and (angular) frequency ω, can be expressed as [30]

$$\mathbf{E}_\theta(\mathbf{r},\omega) = E(\theta,\omega)\hat{\mathbf{p}}(\theta,\omega)e^{i\mathbf{k}(\theta,\omega)\cdot[\mathbf{r}-\mathbf{r}_0(\theta)]}e^{i\phi(\theta)}, \tag{1}$$

where $E(\theta,\omega)$ is a (complex-valued) field amplitude at the excitation point, and

$$\mathbf{k}(\theta,\omega) = k_{\parallel}(\omega)\hat{\mathbf{e}}_{\parallel}(\theta) + k_z(\omega)\hat{\mathbf{e}}_z, \tag{2}$$

$$\hat{\mathbf{p}}(\theta,\omega) = \hat{\mathbf{k}}(\theta,\omega)\times\hat{\mathbf{s}}(\theta) \tag{3}$$

are the wave and normalized polarization vectors, respectively, with $\hat{\mathbf{k}}(\theta,\omega) = \mathbf{k}(\theta,\omega)/|\mathbf{k}(\omega)|$, $\hat{\mathbf{s}}(\theta) = \hat{\mathbf{e}}_z \times \hat{\mathbf{e}}_{\parallel}(\theta)$, and $\hat{\mathbf{e}}_z$ being the Cartesian unit vector along the z axis. Note that the wave-vector magnitude $|\mathbf{k}(\omega)|$ is independent of θ and not equal to the free-space wave number $k_0 = \omega/c$ [43], where c is the speed of light in vacuum. We further take the metal film to be thick enough (e.g., 50–100 nm for Ag), such that the mode overlap across the metal is negligible [43,44]. Thus, the tangential and normal wave-vector components in Eq. (2) read as [28]

$$k_{\parallel}(\omega) = k_0\left[\frac{\epsilon_{\text{r}}(\omega)}{\epsilon_{\text{r}}(\omega)+1}\right]^{1/2}, \tag{4}$$

$$k_z(\omega) = k_0\left[\frac{1}{\epsilon_{\text{r}}(\omega)+1}\right]^{1/2}, \tag{5}$$

where $\epsilon_{\text{r}}(\omega)$ is the (complex-valued) relative electric permittivity of the metal. We stress here that once a suitable plasmonic material in the thick film Kretschmann setup has been chosen, the physical properties of individual SPPs (at a given frequency) are fully determined by the wave-vector components in Eqs. (4) and (5), regardless of the excitation process specifics.

The factor $\phi(\theta)$ in Eq. (1) denotes the phase of the SPP at the excitation point, which is determined by the dynamical phase on plasmon creation. In our case, we assume excitation with a circularly polarized, OAM carrying incident beam [5–9], whereupon due to the spin-orbit coupling effect of the light in plasmon generation [45], the initial phase difference between any two constituent SPPs of the SPPV field takes on the form

$$\phi(\theta_1) - \phi(\theta_2) = m(\theta_1 - \theta_2). \tag{6}$$

Here, $m = s + l$, with s and l being the spin and orbital angular momentum—in units of $\hbar$ per photon—of the circularly polarized, OAM carrying incident beam, respectively.

It follows from the Maxwell equations in vacuum that the corresponding spatial part of the magnetic field for a single SPP in air, at point $\mathbf{r}$ and frequency ω, reads as

$$\mathbf{H}_\theta(\mathbf{r},\omega) = \frac{-k_0(\omega)}{Z_0|\mathbf{k}(\omega)|}E(\theta,\omega)\hat{\mathbf{s}}(\theta)e^{i\mathbf{k}(\theta,\omega)\cdot[\mathbf{r}-\mathbf{r}_0(\theta)]}e^{i\phi(\theta)}. \tag{7}$$

Here, $Z_0 = [\mu_0/\epsilon_0]^{1/2}$ is the free-space impedance and μ_0 and ϵ_0 are the vacuum permeability and permittivity, respectively. In Eq. (7), $\hat{\mathbf{s}}(\theta) = \hat{\mathbf{e}}_z \times \hat{\mathbf{e}}_{\parallel}(\theta) = -\sin\theta\hat{\mathbf{e}}_x + \cos\theta\hat{\mathbf{e}}_y$ is, as before, the unit polarization vector for the magnetic field. Hence the magnetic field for the SPP oscillates only in the xy plane and is always tangential to the excitation circle.

Taking all uniformly distributed SPPs excited on the circular ring into account, the electric and magnetic parts of the SPPV field in air, for $(x^2+y^2)^{1/2} \leqslant a$ and at frequency ω, become

$$\mathbf{E}(\mathbf{r},\omega) = \int_0^{2\pi} \mathbf{E}_\theta(\mathbf{r},\omega) d\theta, \tag{8}$$

$$\mathbf{H}(\mathbf{r},\omega) = \int_0^{2\pi} \mathbf{H}_\theta(\mathbf{r},\omega) d\theta. \tag{9}$$

We next take $\mathbf{E}(\mathbf{r},\omega)$ and $\mathbf{H}(\mathbf{r},\omega)$ in Eqs. (8) and (9) to represent statistical field realizations. The spectral electric and magnetic coherence matrices, which encompass all the second-order stochastic properties of stationary electric and magnetic fields, can then be written as [46]

$$\mathbf{W}^{(\mathrm{E})}(\mathbf{r}_1,\mathbf{r}_2,\omega) = \langle \mathbf{E}^*(\mathbf{r}_1,\omega)\mathbf{E}^{\mathrm{T}}(\mathbf{r}_2,\omega)\rangle, \tag{10}$$

$$\mathbf{W}^{(\mathrm{H})}(\mathbf{r}_1,\mathbf{r}_2,\omega) = \langle \mathbf{H}^*(\mathbf{r}_1,\omega)\mathbf{H}^{\mathrm{T}}(\mathbf{r}_2,\omega)\rangle, \tag{11}$$

where the asterisk, superscript T, and angle brackets denote complex conjugate, matrix transpose, and ensemble average, respectively. It follows from Eqs. (1)–(11) that the spectral electric and magnetic coherence matrices for the SPPV field read

$$\begin{aligned}\mathbf{W}^{(\mathrm{E})}(\mathbf{r}_1,\mathbf{r}_2,\omega) = e^{-2k_\parallel''(\omega)a} \int_0^{2\pi}\int_0^{2\pi} & W(\theta_1,\theta_2,\omega) \\ & \times \hat{\mathbf{p}}^*(\theta_1,\omega)\hat{\mathbf{p}}^{\mathrm{T}}(\theta_2,\omega) \\ & \times e^{i[\mathbf{k}(\theta_2,\omega)\cdot\mathbf{r}_2 - \mathbf{k}^*(\theta_1,\omega)\cdot\mathbf{r}_1]} \\ & \times e^{im(\theta_2-\theta_1)} d\theta_1 d\theta_2,\end{aligned} \tag{12}$$

$$\begin{aligned}\mathbf{W}^{(\mathrm{H})}(\mathbf{r}_1,\mathbf{r}_2,\omega) = \frac{k_0^2(\omega)}{Z_0^2|\mathbf{k}(\omega)|^2} e^{-2k_\parallel''(\omega)a} & \\ \times \int_0^{2\pi}\int_0^{2\pi} & W(\theta_1,\theta_2,\omega)\hat{\mathbf{s}}(\theta_1)\hat{\mathbf{s}}^{\mathrm{T}}(\theta_2) \\ & \times e^{i[\mathbf{k}(\theta_2,\omega)\cdot\mathbf{r}_2 - \mathbf{k}^*(\theta_1,\omega)\cdot\mathbf{r}_1]} \\ & \times e^{im(\theta_2-\theta_1)} d\theta_1 d\theta_2.\end{aligned} \tag{13}$$

Here, $k_\parallel''(\omega)$ denotes the imaginary part of $k_\parallel(\omega)$, which determines the SPP propagation length $l_{\mathrm{SPP}}(\omega) = 1/k_\parallel''(\omega)$, and

$$W(\theta_1,\theta_2,\omega) = \langle E^*(\theta_1,\omega)E(\theta_2,\omega)\rangle \tag{14}$$

is an angular correlation function among the individual SPPs excited at different angular coordinates. The function $W(\theta_1,\theta_2,\omega)$ can be arbitrarily designed within the framework of the recently established "plasmon coherence engineering" paradigm [30].

Equations (12)–(14) represent a stationary polychromatic SPPV field of arbitrary spatial coherence at a metal-air interface with the electromagnetic properties of all individual SPPs fully accounted for. We note that the SPPV fields possess high structural stability with respect to the excitation ring radius variations since the radius a acts effectively merely as a scaling factor of the coherence matrices, and thereby of all derivative quantities. Further, we observe in Eqs. (12) and (13) that once the metal parameters, radius a, and the angular momentum m of the excitation light are known, all elements apart from $W(\theta_1,\theta_2,\omega)$ are specified in the coherence matrices. Thus, the angular SPP correlation function $W(\theta_1,\theta_2,\omega)$ is an additional and essential degree of freedom that can be exploited to control the fundamental physical properties, such as the coherence state, energy density, energy flow, angular momentum, and polarization, of the SPPV fields. This is a demonstration of the power of spatial coherence control to engineer surface electromagnetic fields carrying optical vortices.

III. COHERENT MODE REPRESENTATION

We assume that the angular SPP correlation function possesses circular periodic symmetry and we consider SPP constituents with equal initial intensities. Thus, $W(\theta_1,\theta_2,\omega)$ in Eq. (14) can be expanded into a two-dimensional Fourier series with respect to the angular coordinates as [47]

$$W(\theta_1,\theta_2,\omega) = I_{\mathrm{SPP}}(\omega) \sum_{n=-\infty}^{\infty} \beta_n(\omega) e^{in(\theta_2-\theta_1)}, \tag{15}$$

where $I_{\mathrm{SPP}}(\omega)$ denotes the SPP initial intensity, $\{n\}$ are the mode indices, and $\{\beta_n(\omega)\}$ are the Fourier coefficients. In order to make sure that $W(\theta_1,\theta_2,\omega)$ is a genuine correlation function, $\{\beta_n(\omega)\}$ should be real and non-negative [46]. We note that the expansion in Eq. (15) is essentially a coherent mode representation of the SPP angular correlation function, and hence the Fourier coefficients $\{\beta_n(\omega)\}$ correspond to the modal weights, each representing the amount of energy carried by an individual coherent mode.

The SPPV field is fully coherent if and only if there is only one term in the above series. The field becomes partially coherent with the increase of the number of series terms. In the limiting case of a very large number of modes with identical modal weights [$\beta_n(\omega) = 1$ for all n], Eq. (15) reduces to $W(\theta_1,\theta_2,\omega) = I_{\mathrm{SPP}}(\omega)\delta(\theta_1-\theta_2)$, where $\delta(\cdot)$ is the Dirac delta function. As a consequence, the fields in any pair of angular directions, $\theta_1 \neq \theta_2$, are mutually uncorrelated.

On substituting from Eq. (15) into Eqs. (12) and (13) and integrating over θ, we obtain analytical expressions for the electric and magnetic coherence matrices for the SPPV fields. These can be expressed in terms of the vectorial coherent mode representations as

$$\mathbf{W}^{(\S)}(\mathbf{r}_1,\mathbf{r}_2,\omega) = \sum_{n=-\infty}^{\infty} \xi_n^{(\S)}(\omega)\mathbf{\Phi}_n^{(\S)*}(\mathbf{r}_1,\omega)\mathbf{\Phi}_n^{(\S)\mathrm{T}}(\mathbf{r}_2,\omega), \tag{16}$$

where

$$\mathbf{\Phi}_n^{(\S)}(\mathbf{r},\omega) = \mathbf{\Psi}_n^{(\S)}(\mathbf{r},\omega)/\mathcal{N}_n^{(\S)}(\omega), \tag{17}$$

$$\xi_n^{(\S)}(\omega) = \beta_n(\omega)\pi^2 I_{\mathrm{SPP}}(\omega) e^{-2k_\parallel''(\omega)a} \mathcal{N}_n^{(\S)2}(\omega), \tag{18}$$

are the normalized vector coherent modes and their respective modal weights. The superscript $\S \in (\mathrm{E},\mathrm{H})$ identifies the electric or magnetic field component and $\mathcal{N}_n^{(\S)}(\omega) =$

$[\int_V \mathbf{\Psi}_n^{(\S)\mathrm{T}}(\mathbf{r},\omega)\mathbf{\Psi}_n^{(\S)*}(\mathbf{r},\omega)d^3\mathbf{r}]^{1/2}$ are the normalization factors for the unnormalized vector coherent modes $\mathbf{\Psi}_n^{(\S)}(\mathbf{r},\omega)$, with $\int_V \cdot\, d^3\mathbf{r}$ denoting an integration volume within the SPP excitation region V. We stress that the modal weights $\{\xi_n^{(\S)}(\omega)\}$ are real and nonnegative, and the vector coherent modes $\{\mathbf{\Phi}_n^{(\S)}(\mathbf{r},\omega)\}$ are orthonormal, such that the inner product is given by

$$\int_V \mathbf{\Phi}_{n_1}^{(\S)\mathrm{T}}(\mathbf{r},\omega)\mathbf{\Phi}_{n_2}^{(\S)*}(\mathbf{r},\omega)d^3\mathbf{r} = \delta_{n_1,n_2}, \tag{19}$$

where δ_{n_1,n_2} is the Kronecker delta symbol. In cylindrical coordinates, the unnormalized vector coherent modes are expressed in closed form as (see Appendix A)

$$\begin{aligned}\mathbf{\Psi}_n^{(\mathrm{E})}(\mathbf{r},\omega) = {}& |\mathbf{k}(\omega)|^{-1} e^{ik_z(\omega)z} e^{i(m+n)\varphi}(-ik_z(\omega)\{\mathrm{J}_{m+n+1}[k_\parallel(\omega)\rho] - \mathrm{J}_{m+n-1}[k_\parallel(\omega)\rho]\}\hat{\mathbf{e}}_\rho \\ & - k_z(\omega)\{\mathrm{J}_{m+n+1}[k_\parallel(\omega)\rho] + \mathrm{J}_{m+n-1}[k_\parallel(\omega)\rho]\}\hat{\mathbf{e}}_\varphi + 2k_\parallel(\omega)\mathrm{J}_{m+n}[k_\parallel(\omega)\rho]\hat{\mathbf{e}}_z),\end{aligned} \tag{20}$$

$$\begin{aligned}\mathbf{\Psi}_n^{(\mathrm{H})}(\mathbf{r},\omega) = {}& [Z_0|\mathbf{k}(\omega)|]^{-1} e^{ik_z(\omega)z} e^{i(m+n)\varphi}(k_0(\omega)\{\mathrm{J}_{m+n+1}[k_\parallel(\omega)\rho] + \mathrm{J}_{m+n-1}[k_\parallel(\omega)\rho]\}\hat{\mathbf{e}}_\rho \\ & - ik_0(\omega)\{\mathrm{J}_{m+n+1}[k_\parallel(\omega)\rho] - \mathrm{J}_{m+n-1}[k_\parallel(\omega)\rho]\}\hat{\mathbf{e}}_\varphi),\end{aligned} \tag{21}$$

where (ρ,φ) are cylindrical polar coordinates, $\mathrm{J}_\nu(\cdot)$ is the Bessel function of the first kind and of order ν, and $\hat{\mathbf{e}}_\rho$, $\hat{\mathbf{e}}_\varphi$, $\hat{\mathbf{e}}_z$ form an orthonormal vector set in the cylindrical reference frame. It follows from Eqs. (20) and (21) that any SPPV coherent mode carries a vortex phase $e^{i(m+n)\varphi}$; hence the mode topological charge is determined by the angular momentum $m = l + s$ of the excitation light beam and the mode index n of the angular SPP correlation function. It is also of interest to note that the electric and magnetic coherent modes given by Eqs. (20) and (21) are coupled by Maxwell's equations.

IV. ENERGY DENSITY AND TOTAL ENERGY

The (time-averaged) energy density of a partially coherent electromagnetic field is given by [46]

$$w(\mathbf{r},\omega) = \tfrac{1}{4}[\epsilon_0 \operatorname{tr}\mathbf{W}^{(\mathrm{E})}(\mathbf{r},\mathbf{r},\omega) + \mu_0 \operatorname{tr}\mathbf{W}^{(\mathrm{H})}(\mathbf{r},\mathbf{r},\omega)], \tag{22}$$

where tr denotes the matrix trace. On substituting from Eq. (16) the vectorial coherent mode representations for the coherence matrices into Eq. (22), we obtain the SPPV field energy density in terms of the energy densities carried by the individual vector coherent modes as

$$\begin{aligned}w(\mathbf{r},\omega) = \frac{1}{4}\sum_{n=-\infty}^{\infty} \big[& \epsilon_0 \xi_n^{(\mathrm{E})}(\omega)\big|\mathbf{\Phi}_n^{(\mathrm{E})}(\mathbf{r},\omega)\big|^2 \\ & + \mu_0 \xi_n^{(\mathrm{H})}(\omega)\big|\mathbf{\Phi}_n^{(\mathrm{H})}(\mathbf{r},\omega)\big|^2\big].\end{aligned} \tag{23}$$

The total energy of an SPPV field can then be determined by volume integration of the energy density within the SPP excitation region or by summing the energies carried by the individual modes. Based on the orthonormality of the vector coherent modes, Eq. (19), the two alternative approaches lead to the same result

$$\mathcal{W}(\omega) = \int_V w(\mathbf{r},\omega)d^3\mathbf{r} = \sum_{n=-\infty}^{\infty} \xi_n(\omega), \tag{24}$$

where $\xi_n(\omega) = [\epsilon_0 \xi_n^{(\mathrm{E})}(\omega) + \mu_0 \xi_n^{(\mathrm{H})}(\omega)]/4$ is the energy carried by the vector coherent mode of index n. The SPPV field energy density control by optical coherence will be illustrated later in Fig. 2.

V. GLOBAL DEGREE OF COHERENCE

In analogy with the electric global degree of coherence [48] and taking account of the magnetic global degree of coherence [49], the (squared) global degree of coherence for a partially coherent electromagnetic field can be defined as

$$\mathcal{G}^2(\omega) = \frac{\int_{V_1,V_2} \mathcal{F}^2(\mathbf{r}_1,\mathbf{r}_2,\omega)d^3\mathbf{r}_1 d^3\mathbf{r}_2}{\mathcal{W}^2(\omega)}, \tag{25}$$

where

$$\begin{aligned}\mathcal{F}(\mathbf{r}_1,\mathbf{r}_2,\omega) = {}& \frac{\epsilon_0}{4}\|\mathbf{W}^{(\mathrm{E})}(\mathbf{r}_1,\mathbf{r}_2,\omega)\|_\mathrm{F} \\ & + \frac{\mu_0}{4}\|\mathbf{W}^{(\mathrm{H})}(\mathbf{r}_1,\mathbf{r}_2,\omega)\|_\mathrm{F},\end{aligned} \tag{26}$$

where $\|\cdot\|_\mathrm{F}$ is the Frobenius norm. The global degree of coherence is a useful quantity to characterize how coherent an electromagnetic field is on average within a limited volume. It is bounded as $0 < \mathcal{G}(\omega) \leqslant 1$, with the upper limit corresponding to a fully coherent field and the lower limit to a virtually incoherent field, while the intermediate values describe partially coherent fields. It follows from Eqs. (16)–(21) and (24)–(26) that the global degree of coherence of an SPPV field is given by the expression

$$\mathcal{G}(\omega) = \frac{\left[\sum_{n=-\infty}^{\infty} \xi_n^2(\omega)\right]^{1/2}}{\sum_{n=-\infty}^{\infty} \xi_n(\omega)}. \tag{27}$$

We can infer from Eq. (27) that $\mathcal{G}(\omega) = 1$ if and only if a single coherent mode is excited, whereby the SPPV field is fully coherent. As the number of excited modes increases, the global degree of coherence is reduced and the SPPV field becomes partially coherent.

VI. ANGULAR MOMENTUM

To assess the angular momentum of the SPPV field, we employ a canonical approach [50], which is more suitable for the description of the angular momentum properties of light than simply using the Poynting vector components. This is because the canonical approach can separately address spin and orbital degrees of freedom of light, making these canonical quantities directly measurable [51,52]. In the canonical picture, the

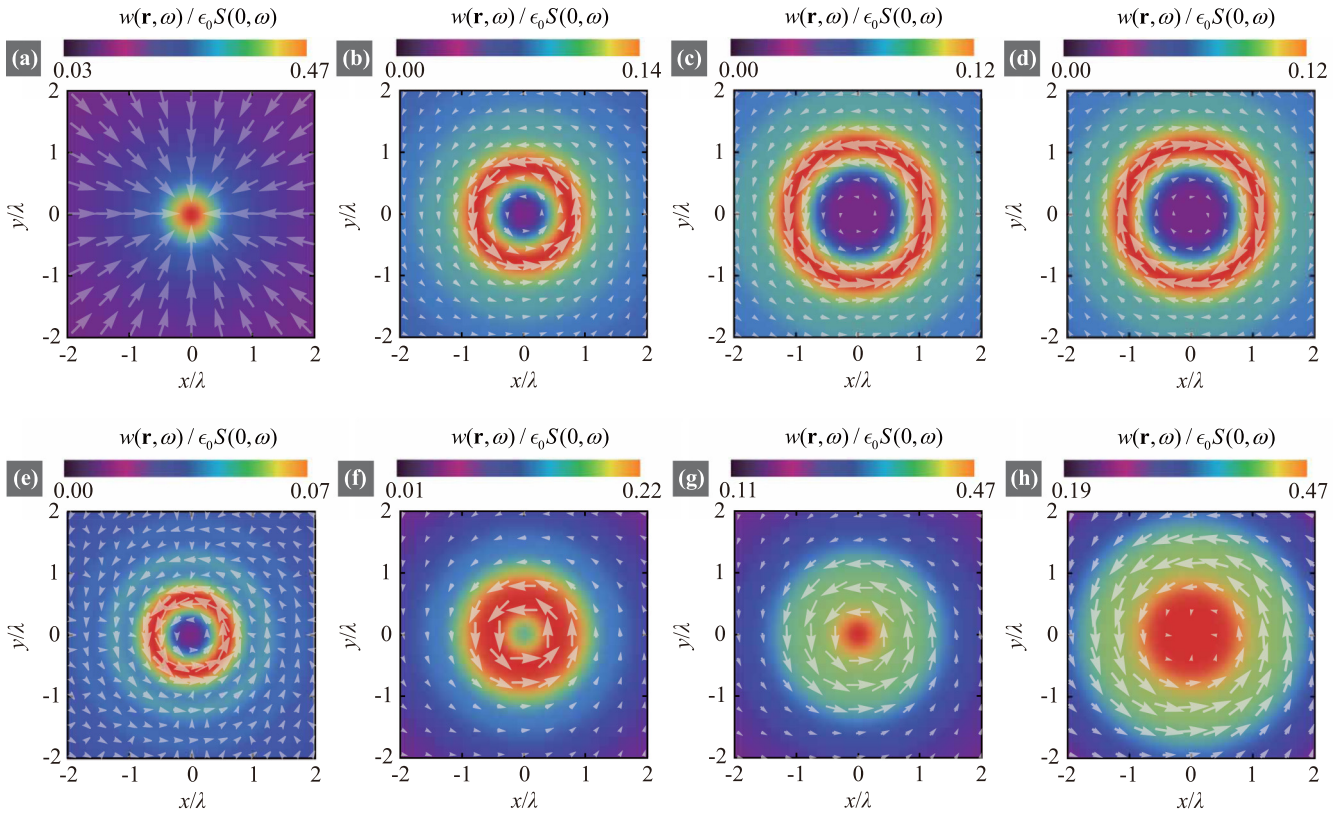

FIG. 2. Energy density $w(\mathbf{r},\omega)$ and the in-plane Poynting vector components, $[\langle P(\mathbf{r},\omega)\rangle_\rho, \langle P(\mathbf{r},\omega)\rangle_\varphi]$, for SPPV fields at a gold-air interface at the free-space wavelength $\lambda = 632.8$ nm, for a varying number of coherent modes N and average OAM $\mathcal{L}(\omega)$: (a) $N = 3$ and $\beta_n(\omega) = 1$ for $n \in (-3,-2,-1)$, $\mathcal{L}(\omega) = 0$; (b) $N = 3$, $\beta_n(\omega) = 1$ for $n \in (1,2,3)$, $\mathcal{L}(\omega) = 4\hbar\hat{\mathbf{e}}_z$; (c) $N = 3$, $\beta_n(\omega) = 1$ for $n \in (3,4,5)$, and $\mathcal{L}(\omega) = 6\hbar\hat{\mathbf{e}}_z$; (d) $N = 3$, $\beta_n(\omega) = 1$ for $n \in (-9,-8,-7)$, and $\mathcal{L}(\omega) = -6\hbar\hat{\mathbf{e}}_z$; (e) $N = 1$, $\beta_n(\omega) = 1$ for $n = 1$, and OAM $\mathcal{L}(\omega) = 3\hbar\hat{\mathbf{e}}_z$; (f) $N = 5$, $\beta_n(\omega) = 1$ for $n \in (-1,\ldots,3)$, and $\mathcal{L}(\omega) = 3\hbar\hat{\mathbf{e}}_z$; (g) $N = 9$, $\beta_n(\omega) = 1$ for $n \in (-3,\ldots,5)$, and $\mathcal{L}(\omega) = 3\hbar\hat{\mathbf{e}}_z$; (h) $N = 15$, $\beta_n(\omega) = 1$ for $n \in (-6,\ldots,8)$, and $\mathcal{L}(\omega) = 3\hbar\hat{\mathbf{e}}_z$. Note that the excitation light angular momentum is fixed at $m = 2$ and the excitation ring radius is set to $a = l_{\mathrm{SPP}}(\lambda)$. The energy density $w(\mathbf{r},\omega)$ is normalized with respect to $\epsilon_0 S(0,\omega)$. The relative permittivity of gold is from empirical data in [53].

(time-averaged) OAM and spin angular momentum (SAM) densities of a monochromatic optical field are given by [50]

$$\mathbf{l}(\mathbf{r},\omega) = \mathbf{r} \times \mathbf{p}(\mathbf{r},\omega), \tag{28}$$

$$\mathbf{s}(\mathbf{r},\omega) = \frac{1}{4\omega}\mathrm{Im}\{\epsilon_0 \mathbf{E}^*(\mathbf{r},\omega) \times \mathbf{E}(\mathbf{r},\omega) + \mu_0 \mathbf{H}^*(\mathbf{r},\omega) \times \mathbf{H}(\mathbf{r},\omega)\}, \tag{29}$$

respectively. The orbital (or canonical) linear momentum density $\mathbf{p}(\mathbf{r},\omega)$ in Eq. (28) is defined as

$$\mathbf{p}(\mathbf{r},\omega) = \frac{1}{4\omega}\mathrm{Im}\{\epsilon_0 \mathbf{E}^*(\mathbf{r},\omega) \cdot [\nabla]\mathbf{E}(\mathbf{r},\omega) + \mu_0 \mathbf{H}^*(\mathbf{r},\omega) \cdot [\nabla]\mathbf{H}(\mathbf{r},\omega)\}, \tag{30}$$

where we use the notation $\mathbf{A} \cdot [\nabla]\mathbf{B} = A_x \nabla B_x + A_y \nabla B_y + A_z \nabla B_z$. For a partially coherent electromagnetic field, the OAM and SAM densities can be obtained through ensemble averaging in Eqs. (28)–(30). Furthermore, by applying the vector coherent mode representation of Sec. III, we find the OAM density of an SPPV field as

$$\langle \mathbf{l}(\mathbf{r},\omega)\rangle = \mathbf{r} \times \langle \mathbf{p}(\mathbf{r},\omega)\rangle, \tag{31}$$

with

$$\langle \mathbf{p}(\mathbf{r},\omega)\rangle = \frac{1}{4\omega}\mathrm{Im}\left[\epsilon_0 \sum_{n=-\infty}^{\infty} \xi_n^{(\mathrm{E})}(\omega)\boldsymbol{\Phi}_n^{(\mathrm{E})*}(\mathbf{r},\omega) \cdot [\nabla]\boldsymbol{\Phi}_n^{(\mathrm{E})}(\mathbf{r},\omega) + \mu_0 \sum_{n=-\infty}^{\infty} \xi_n^{(\mathrm{H})}(\omega)\boldsymbol{\Phi}_n^{(\mathrm{H})*}(\mathbf{r},\omega) \cdot [\nabla]\boldsymbol{\Phi}_n^{(\mathrm{H})}(\mathbf{r},\omega)\right], \tag{32}$$

and the SAM density of an SPPV field as

$$\langle \mathbf{s}(\mathbf{r},\omega)\rangle = \frac{1}{4\omega}\mathrm{Im}\left[\epsilon_0 \sum_{n=-\infty}^{\infty} \xi_n^{(\mathrm{E})}(\omega)\boldsymbol{\Phi}_n^{(\mathrm{E})*}(\mathbf{r},\omega) \times \boldsymbol{\Phi}_n^{(\mathrm{E})}(\mathbf{r},\omega) + \mu_0 \sum_{n=-\infty}^{\infty} \xi_n^{(\mathrm{H})}(\omega)\boldsymbol{\Phi}_n^{(\mathrm{H})*}(\mathbf{r},\omega) \times \boldsymbol{\Phi}_n^{(\mathrm{H})}(\mathbf{r},\omega)\right]. \tag{33}$$

Here, we are interested in the average angular momentum per photon, which is given by the total (integrated) angular momentum divided by the total number of photons in the

SPPV excitation region. Thus, the average OAM $\boldsymbol{\mathcal{L}}(\omega)$ and the average SAM $\boldsymbol{\mathcal{S}}(\omega)$ associated with a photon in the SPPV field can be expressed as

$$\boldsymbol{\mathcal{L}}(\omega) = \langle \mathbf{L}(\omega)\rangle / N_{\mathrm{ph}}, \tag{34}$$

$$\boldsymbol{\mathcal{S}}(\omega) = \langle \mathbf{S}(\omega)\rangle / N_{\mathrm{ph}}, \tag{35}$$

where the total OAM, SAM, and photon number within the SPPV field excitation region are respectively given by

$$\langle \mathbf{L}(\omega)\rangle = \int_{\mathrm{V}} \langle \mathbf{l}(\mathbf{r},\omega)\rangle d^3\mathbf{r}, \tag{36}$$

$$\langle \mathbf{S}(\omega)\rangle = \int_{\mathrm{V}} \langle \mathbf{s}(\mathbf{r},\omega)\rangle d^3\mathbf{r}, \tag{37}$$

$$N_{\mathrm{ph}} = \mathcal{W}(\omega)/(\hbar\omega). \tag{38}$$

It then follows from Eqs. (17)–(21), (24), (31), (32), (34), (36), and (38) that the average OAM per photon of the SPPV field is

$$\boldsymbol{\mathcal{L}}(\omega) = \frac{\sum_{n=-\infty}^{\infty}(m+n)\xi_n(\omega)}{\sum_{n=-\infty}^{\infty}\xi_n(\omega)}\hbar\hat{\mathbf{e}}_z. \tag{39}$$

The derivation of this general result can be found in Appendix B. Several instructive conclusions can be drawn from Eq. (39).

(i) The average OAM $\boldsymbol{\mathcal{L}}(\omega)$ is strictly parallel (or antiparallel) with the z axis since the radial and azimuthal components vanish when integrating the local OAM density $\langle \mathbf{l}(\mathbf{r},\omega)\rangle$ over the plasmon excitation region. This behavior is rather intuitive considering the axial symmetry of the SPPV excitation geometry and is quite different from that of a propagating vortex beam [3], for which the average OAM is parallel to the propagation direction. The average SPPV OAM, on the other hand, is perpendicular to the SPP propagation direction.

(ii) The average OAM of a fully coherent SPPV field, composed of a single vector coherent mode $\boldsymbol{\Phi}_{n_0}^{(\S)}(\mathbf{r},\omega)$, is $\boldsymbol{\mathcal{L}}(\omega) = (m+n_0)\hbar\hat{\mathbf{e}}_z$. This is a quite obvious result due to the spin-orbit coupling effect of light upon fully coherent SPP excitation [45].

(iii) The average OAM of a partially coherent SPPV field can be arbitrarily controlled by the angular SPP correlation function. In particular, whenever $\{\xi_n(\omega)\}$ satisfy the condition $\xi_n(\omega) = \xi_{2p-n-2m}(\omega)$, where p is an arbitrary integer, the average OAM is $\boldsymbol{\mathcal{L}}(\omega) = p\hbar\hat{\mathbf{e}}_z$ (see Appendix B for the derivation). Hence, if $\xi_n(\omega) = \xi_{-n-2m}(\omega)$, the SPPV field carries no OAM, $\boldsymbol{\mathcal{L}}(\omega) = 0$. On the other hand, if $\xi_n(\omega) = \xi_{-n}(\omega)$, the average SPPV OAM is $m\hbar\hat{\mathbf{e}}_z$, i.e, it is determined solely by the angular momentum of the excitation light.

(iv) For a fully incoherent SPPV field, the relation $\xi_n(\omega) = \xi_{-n-2m}(\omega)$ holds (see Appendix C for details), implying absence of OAM. This rather obvious result formally follows from the Bessel function property $\mathrm{J}_{-n}(x) = (-1)^n\mathrm{J}_n(x)$ and from the fact that the modal weights $\{\beta_n(\omega)\}$ in the SPPV coherent mode representation are all equal to unity in the incoherent case (see Sec. III).

In addition to exercising arbitrary control of the average SPPV OAM, we can freely tailor the SPPV global degree of coherence by adjusting the SPP angular correlation function, as is indicated by Eq. (27). It follows that an SPPV field with a given OAM may have a variable global degree of coherence or vice versa.

Next, we examine the average SAM of an SPPV field with the help of Eqs. (17)–(21), (24), (33), (35), (37), and (38). We find that the average SPPV SAM is also normal to the metal-air interface and it can be expressed as

$$\boldsymbol{\mathcal{S}}(\omega) = \frac{\int_{\mathrm{V}} S_z(\mathbf{r},\omega)d^3\mathbf{r}}{\mathcal{W}(\omega)}\hbar\omega\hat{\mathbf{e}}_z. \tag{40}$$

Here, the z component of the SAM density reads

$$S_z(\mathbf{r},\omega) = \frac{\epsilon_0}{8\omega}\frac{|k_z(\omega)|^2 + k_0^2(\omega)}{|\mathbf{k}(\omega)|^2}S(z,\omega)\sum_{n=-\infty}^{\infty}\beta_n(\omega) \times [|\mathrm{J}_{m+n+1}[k_\parallel(\omega)\rho]|^2 - |\mathrm{J}_{m+n-1}[k_\parallel(\omega)\rho]|^2], \tag{41}$$

where

$$S(z,\omega) = 4\pi^2 I_{\mathrm{SPP}}(\omega)e^{-2k_\parallel''(\omega)a - 2k_z''(\omega)z}, \tag{42}$$

and $k_z''(\omega)$ is the imaginary part of $k_z(\omega)$. It is quite instructive to observe by looking at Eqs. (40) and (41) that the average SPPV SAM behavior is closely linked to that of the OAM. Indeed, in the absence of OAM, we have $\xi_n(\omega) = \xi_{-n-2m}(\omega)$, and it follows at once from Eq. (41) that the SAM vanishes as well. For an SPPV field carrying a nonzero OAM, the magnitude and direction of its SAM can be controlled by the SPP angular correlation function for a given magnitude of the angular momentum m. The physics behind this SPPV SAM behavior is rooted in the SPPV polarization state distribution, which will be examined in detail in Sec. VIII.

VII. ENERGY FLOW

The SPPV energy flow can be studied by considering an ensemble average of the (time-averaged) Poynting vector in the space-frequency representation, viz.,

$$\langle \mathbf{P}(\mathbf{r},\omega)\rangle = \tfrac{1}{2}\mathrm{Re}\langle \mathbf{E}(\mathbf{r},\omega)\times\mathbf{H}^*(\mathbf{r},\omega)\rangle. \tag{43}$$

On substituting from Eqs. (1)–(7) and (15) into Eq. (43), we obtain for the SPPV field (see Appendix D for the derivation)

$$\langle \mathbf{P}(\mathbf{r},\omega)\rangle = \frac{k_0(\omega)S(z,\omega)}{4Z_0|\mathbf{k}(\omega)|^2}\mathrm{Re}[\mathcal{P}_\rho(\rho,\omega)\hat{\mathbf{e}}_\rho + \mathcal{P}_\varphi(\rho,\omega)\hat{\mathbf{e}}_\varphi + \mathcal{P}_z(\rho,\omega)\hat{\mathbf{e}}_z], \tag{44}$$

where the corresponding components read

$$\mathcal{P}_\rho(\rho,\omega) = ik_\parallel(\omega)\sum_{n=-\infty}^{\infty}\beta_n(\omega)\mathrm{J}_{m+n}[k_\parallel(\omega)\rho] \times \{\mathrm{J}_{m+n-1}^*[k_\parallel(\omega)\rho] - \mathrm{J}_{m+n+1}^*[k_\parallel(\omega)\rho]\}, \tag{45}$$

$$\mathcal{P}_\varphi(\rho,\omega) = \frac{1}{\rho}\frac{2k_\parallel(\omega)}{k_\parallel^*(\omega)}\sum_{n=-\infty}^{\infty}\beta_n(\omega) \times (m+n)|\mathrm{J}_{m+n}[k_\parallel(\omega)\rho]|^2, \tag{46}$$

$$\mathcal{P}_z(\rho,\omega) = k_z(\omega)\sum_{n=-\infty}^{\infty}\beta_n(\omega) \times\{|\mathrm{J}_{m+n-1}[k_\parallel(\omega)\rho]|^2 + |\mathrm{J}_{m+n+1}[k_\parallel(\omega)\rho]|^2\}. \tag{47}$$

Equations (44)–(47) reveal several salient features of the SPPV energy flow. First, the normal component of the Poynting vector $\langle P(\mathbf{r},\omega)\rangle_z \leqslant 0$ due to the real part of $k_z(\omega)$ being negative. It follows that the SPPV energy flows toward the metal surface, except for some special points where $\langle P(\mathbf{r},\omega)\rangle_z = 0$ and the energy flow is along the metal-air interface. Second, the magnitude and direction of the Poynting vector projection $\langle P(\mathbf{r},\omega)\rangle_\varphi$ onto the interface plane are determined by the average OAM of the field. For example, when the field carries no average OAM, we have $\xi_n(\omega) = \xi_{-n-2m}(\omega)$, and therefore $\langle P(\mathbf{r},\omega)\rangle_\varphi = 0$, implying that the energy flow along the interface only has a radial component. However, for the fields that carry a nonzero average OAM, the azimuthal component $\langle P(\mathbf{r},\omega)\rangle_\varphi$ is, in general, present as well. Moreover, the spatial $1/\rho$ dependence of the azimuthal component $\langle P(\mathbf{r},\omega)\rangle_\varphi$ indicates the helical distribution of the energy flow at the metal-air interface.

To illustrate the SPPV energy flow along the metal-air interface, we display in Figs. 2(a)–2(d), with white arrows in the top-row panels, the spatial behavior of the Poynting vector $[\langle P(\mathbf{r},\omega)\rangle_\rho, \langle P(\mathbf{r},\omega)\rangle_\varphi]$ in a gold-air interface plane for the SPPV fields with the same number of vector coherent modes but with a different average OAM. The free-space wavelength is $\lambda = 632.8$ nm and the excitation ring radius is taken to be $a = l_{\mathrm{SPP}}(\lambda)$. The figure background shows the corresponding energy densities, which are calculated using Eqs. (17)–(21) and (23). We note here that the angular momentum of the excitation light is fixed to $m = 2$ and thus the average OAM and coherence of the SPPV fields are completely controlled by the SPP angular correlation function. We infer from Fig. 2(a) that in the absence of the OAM, the in-plane energy flow is purely radial towards the ring center. At the same time, the energy density shows a hot spot at the center, which is similar to that for the partially coherent axiconic SPP fields [37]. However, Figs. 2(b)–2(d) illustrate that for the fields carrying nonzero average OAM, the in-plane energy flow displays a circular pattern around the ring center, resulting in doughnutlike energy density distributions at the metal-air interface. The energy circulation direction is determined by the sign of the average OAM: a positive OAM induces a counterclockwise energy circulation, while the energy flow direction is reversed for a negative OAM [see Fig. 2(d)]. We emphasize, however, that the in-plane energy flow patterns are not strictly azimuthal due to the presence of a nonzero radial component of the Poynting vector.

To explore the influence of the SPPV coherence on the energy flow patterns, we display in Figs. 2(e)–2(h) the in-plane Poynting vectors $[\langle P(\mathbf{r},\omega)\rangle_\rho, \langle P(\mathbf{r},\omega)\rangle_\varphi]$ and the corresponding energy densities $w(\mathbf{r},\omega)$ for the SPPV fields of the same average OAM but a different number of coherent modes at the gold-air interface at the free-space wavelength $\lambda = 632.8$ nm, with the excitation ring radius taken to be $a = l_{\mathrm{SPP}}(\lambda)$. We find that the in-plane energy flow exhibits circular patterns in the counterclockwise direction as the SPPV fields carry the same positive average OAM. However, the characteristic doughnutlike energy density distribution generally disappears as the number of coherent modes is increased, implying reduced spatial coherence. For example, when the number of modes reaches 15 [Fig. 2(h)], the energy density displays a flat-top profile at the metal surface. This is due to partially impaired interference among partially coherent SPP components.

From the energy density and flow distributions of partially coherent SPPV fields in Fig. 2, we may predict that optical coherence can be employed to dynamically control optical trapping of nanoparticles in the SPPV fields. For instance, by modifying the optical coherence, the energy density of the SPPV field may be modulated, generating a Gaussian, dark-hollow, or flat-top profile. Thus, the optical force of the trapping system, induced by the gradient of the energy density profile, will be dynamically adjusted, and therefore different kinds of particles may be trapped or sorted. In addition, the effective trapping range of the optical gradient force can be enhanced by varying the optical coherence. We further find that the coherence-induced reversal of energy flow may be used in the control of the particle rotation.

VIII. POLARIZATION STATE

The polarization properties characterizing the SPPV fields are determined by the electric and magnetic polarization matrices. Here, we focus on polarization states of the SPPV electric fields which can be inferred from $\mathbf{\Lambda}^{(\mathrm{E})}(\mathbf{r},\omega) = \mathbf{W}^{(\mathrm{E})}(\mathbf{r},\mathbf{r},\omega)$. As the SPPV electric fields have three nonzero components, we must employ a three-dimensional formalism to describe their degree of polarization using, for instance, the definition [54]

$$P(\mathbf{r},\omega) = \left[\frac{3}{2}\frac{\mathrm{tr}\,\mathbf{\Lambda}^{(\mathrm{E})2}(\mathbf{r},\omega)}{\mathrm{tr}^2\,\mathbf{\Lambda}^{(\mathrm{E})}(\mathbf{r},\omega)} - \frac{1}{2}\right]^{1/2}. \tag{48}$$

It readily follows from Eqs. (16)–(20) as well as (48) that $P(\mathbf{r},\omega) = 1$ in the fully coherent limit, indicating that fully coherent SPPV fields are completely polarized everywhere. Interestingly, we also find the fields to remain highly polarized within the SPP excitation region as their degree of coherence is reduced all the way down to a nearly incoherent limit. This feature makes the SPPV fields similar to $(1+1)$D partially coherent SPP fields and the physics behind the remarkable resilience of their polarization to coherence reduction was discussed elsewhere [30,37].

To examine the local polarization states of the SPPV fields, we first study the ratio of the tangential to normal components of their electric polarization matrix

$$\eta(\mathbf{r},\omega) = \frac{\Lambda^{(\mathrm{E})}_{xx}(\mathbf{r},\omega) + \Lambda^{(\mathrm{E})}_{yy}(\mathbf{r},\omega)}{\Lambda^{(\mathrm{E})}_{zz}(\mathbf{r},\omega)}. \tag{49}$$

This ratio will show whether the field is predominantly polarized along the normal to or in the plane of the interface. For example, at the locations such that $\eta(\mathbf{r},\omega) \ll 1$, an SPPV field is polarized along the normal direction; on the other hand, at the points where $\eta(\mathbf{r},\omega) \gg 1$, the field is polarized in the interface plane. It follows from Eqs. (16)–(20) and (49) that

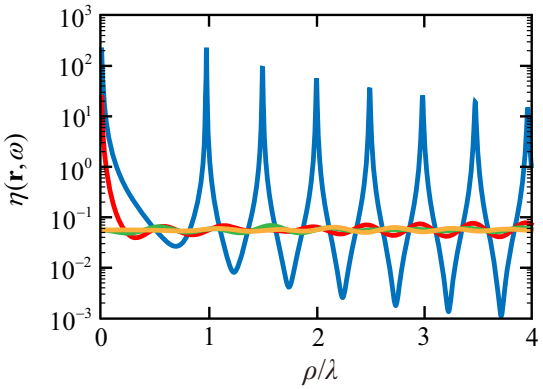

FIG. 3. Ratio $\eta(\mathbf{r},\omega)$ as a function of the radial distance ρ for SPPV fields of average OAM $\boldsymbol{\mathcal{L}}(\omega) = 3\hbar\hat{\mathbf{e}}_z$ at a gold-air interface at $\lambda = 632.8$ nm, with a variable number N of coherent modes: (blue) $N = 1$ and $\beta_n(\omega) = 1$ for $n = 1$; (red) $N = 5$ and $\beta_n(\omega) = 1$ for $n \in (-1, \ldots, 3)$; (green) $N = 9$ and $\beta_n(\omega) = 1$ for $n \in (-3, \ldots, 5)$; (yellow) $N = 15$ and $\beta_n(\omega) = 1$ for $n \in (-6, \ldots, 8)$. Note that the excitation light angular momentum is fixed to $m = 2$. The relative permittivity of gold is from empirical data in [53].

$\eta(\mathbf{r},\omega)$ can be written as

$$\eta(\mathbf{r},\omega) = \frac{|k_z(\omega)|^2}{2|k_\parallel(\omega)|^2}\left\{\sum_{n=-\infty}^{\infty}\beta_n(\omega)|\mathrm{J}_{m+n}[k_\parallel(\omega)\rho]|^2\right\}^{-1} \times \sum_{n=-\infty}^{\infty}\beta_n(\omega)\{|\mathrm{J}_{m+n+1}[k_\parallel(\omega)\rho]|^2 + |\mathrm{J}_{m+n-1}[k_\parallel(\omega)\rho]|^2\}. \tag{50}$$

It follows at once from Eq. (50) that $\eta(\mathbf{r},\omega)$ is independent of position along the z axis. Therefore, we display in Fig. 3 the ratio $\eta(\mathbf{r},\omega)$ as a function of the radial distance ρ for SPPV fields of average OAM equal to $\boldsymbol{\mathcal{L}}(\omega) = 3\hbar\hat{\mathbf{e}}_z$ and of different coherence states at a gold-air interface at $\lambda = 632.8$ nm. It can be seen from the figure that $\eta(\mathbf{r},\omega)$ rapidly alternates between very small and very large values in high coherence regions of SPPV fields, causing the polarization direction to rapidly switch between the normal and tangential to the interface. On the contrary, $\eta(\mathbf{r},\omega)$ is a slowly varying function with a magnitude much smaller than unity for nearly incoherent SPPV fields, implying that such SPPV fields are highly polarized along the normal direction. In particular, it readily follows from Eq. (50) that $\eta(\mathbf{r},\omega) = |k_z(\omega)|^2/|k_\parallel(\omega)|^2 \ll 1$ for completely incoherent SPPV fields, implying that they are indeed highly polarized along the normal direction.

Next, we consider only the polarization component in the interface plane, whereby the polarization properties can be analyzed in terms of the Stokes parameters $\Lambda_j(\mathbf{r},\omega) = \mathrm{tr}[\boldsymbol{\Lambda}_\mathrm{t}(\mathbf{r},\omega)\boldsymbol{\sigma}_j]$ with $j \in (0, \ldots, 3)$, where $\boldsymbol{\Lambda}_\mathrm{t}(\mathbf{r},\omega)$ is a 2×2 polarization matrix in the interface plane, $\boldsymbol{\sigma}_0$ is the 2×2 unit matrix, and $\boldsymbol{\sigma}_1, \boldsymbol{\sigma}_2, \boldsymbol{\sigma}_3$ are the three Pauli matrices. The Stokes parameters are real and have clear physical interpretations [55]. Equations (16)–(20) yield the Stokes parameters of the SPPV fields straightforwardly as

$$\Lambda_0(\mathbf{r},\omega) = \frac{1}{2}S(z,\omega)\frac{|k_z(\omega)|^2}{|\mathbf{k}(\omega)|^2}\sum_{n=-\infty}^{\infty}\beta_n(\omega) \times [|\mathrm{J}_{m+n+1}[k_\parallel(\omega)\rho]|^2 + |\mathrm{J}_{m+n-1}[k_\parallel(\omega)\rho]|^2], \tag{51}$$

$$\Lambda_1(\mathbf{r},\omega) = S(z,\omega)\frac{-|k_z(\omega)|^2}{|\mathbf{k}(\omega)|^2}\sum_{n=-\infty}^{\infty}\beta_n(\omega) \times (\cos 2\varphi\,\mathrm{Re}\{\mathrm{J}^*_{m+n+1}[k_\parallel(\omega)\rho]\mathrm{J}_{m+n-1}[k_\parallel(\omega)\rho]\} - \sin 2\varphi\,\mathrm{Im}\{\mathrm{J}^*_{m+n+1}[k_\parallel(\omega)\rho]\mathrm{J}_{m+n-1}[k_\parallel(\omega)\rho]\}), \tag{52}$$

$$\Lambda_2(\mathbf{r},\omega) = S(z,\omega)\frac{-|k_z(\omega)|^2}{|\mathbf{k}(\omega)|^2}\sum_{n=-\infty}^{\infty}\beta_n(\omega) \times (\sin 2\varphi\,\mathrm{Re}\{\mathrm{J}^*_{m+n+1}[k_\parallel(\omega)\rho]\mathrm{J}_{m+n-1}[k_\parallel(\omega)\rho]\} + \cos 2\varphi\,\mathrm{Im}\{\mathrm{J}^*_{m+n+1}[k_\parallel(\omega)\rho]\mathrm{J}_{m+n-1}[k_\parallel(\omega)\rho]\}), \tag{53}$$

$$\Lambda_3(\mathbf{r},\omega) = \frac{1}{2}S(z,\omega)\frac{|k_z(\omega)|^2}{|\mathbf{k}(\omega)|^2}\sum_{n=-\infty}^{\infty}\beta_n(\omega) \times [|\mathrm{J}_{m+n+1}[k_\parallel(\omega)\rho]|^2 - |\mathrm{J}_{m+n-1}[k_\parallel(\omega)\rho]|^2], \tag{54}$$

where $\Lambda_0(\mathbf{r},\omega)$ describes the in-plane spectral density (average intensity) at $(\mathbf{r},\omega)$, while $\Lambda_1(\mathbf{r},\omega)$, $\Lambda_2(\mathbf{r},\omega)$, and $\Lambda_3(\mathbf{r},\omega)$ specify the differences between the x- and y-polarized, $+\pi/4$ and $-\pi/4$ linearly polarized, and right and left circularly polarized average spectral densities of the in-plane SPPV field component. Thus, the SPPV field's state of in-plane polarization is completely determined by $\Lambda_1(\mathbf{r},\omega)$, $\Lambda_2(\mathbf{r},\omega)$, and $\Lambda_3(\mathbf{r},\omega)$. We then consider a polarization state of an SPPV field with no average OAM by assuming that $\xi_n(\omega) = \xi_{-n-2m}(\omega)$ holds in Eqs. (52)–(54). It follows that $\Lambda_3(\mathbf{r},\omega) = 0$ and $\Lambda_1(\mathbf{r},\omega)/\Lambda_2(\mathbf{r},\omega) = \cot 2\varphi$, implying that the in-plane SPPV field component is strictly radially polarized [see Fig. 4(a)]. Next, for the SPPV fields with a nonzero average OAM, we find that $\Lambda_3(\mathbf{r},\omega) \neq 0$, which indicates that the fields have localized regions of circular polarization. This is the reason why nonzero average OAM fields carry SAM as well.

In Fig. 4, we display the polarization state distribution for SPPV fields of different coherence states and average OAM at a gold-air interface at $\lambda = 632.8$ nm. The top left panel of Fig. 4 demonstrates that SPPV fields with no average OAM are radially polarized, making their polarization and energy flow patterns quite similar [cf. Fig. 2(a)]. By the same token, the in-plane components of OAM carrying SPPV fields are seen to be right or left elliptically polarized. Further, as the average OAM flips sign, the right and left elliptically polarized regions switch places [see Fig. 2(c) and 2(d)], thereby causing the field SAM to change its direction. In the bottom panels of Fig. 4, the SPPV fields have the same average OAM, but different coherence properties. We find

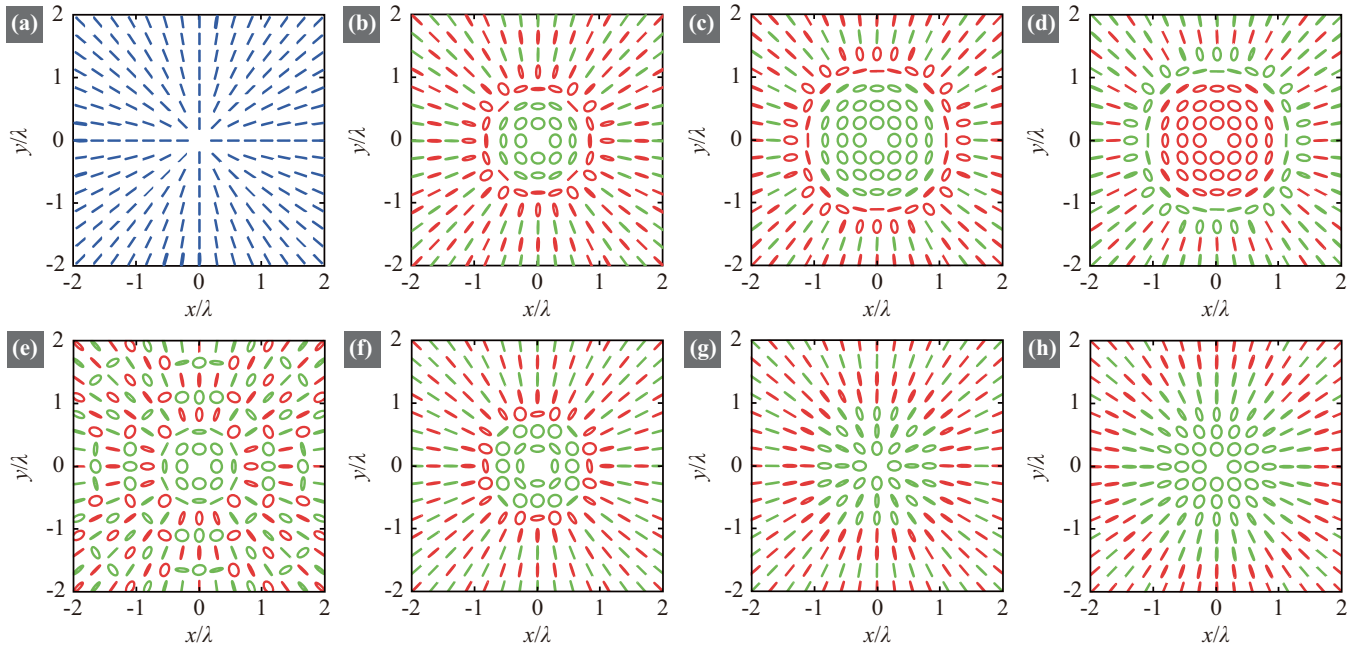

FIG. 4. Polarization state distribution of the in-plane SPPV electric field component at a gold-metal interface at $\lambda = 632.8$ nm with a variable number of coherent modes N and average OAM $\boldsymbol{\mathcal{L}}(\omega)$: (a) $N = 3$, $\beta_n(\omega) = 1$ for $n \in (-3, -2, -1)$, and $\boldsymbol{\mathcal{L}}(\omega) = 0$; (b) $N = 3$, $\beta_n(\omega) = 1$ for $n \in (1, 2, 3)$, and $\boldsymbol{\mathcal{L}}(\omega) = 4\hbar\hat{\mathbf{e}}_z$; (c) $N = 3$, $\beta_n(\omega) = 1$ for $n \in (3, 4, 5)$, and $\boldsymbol{\mathcal{L}}(\omega) = 6\hbar\hat{\mathbf{e}}_z$; (d) $N = 3$, $\beta_n(\omega) = 1$ for $n \in (-9, -8, -7)$, and $\boldsymbol{\mathcal{L}}(\omega) = -6\hbar\hat{\mathbf{e}}_z$; (e) $N = 1$, $\beta_n(\omega) = 1$ for $n = 1$, and $\boldsymbol{\mathcal{L}}(\omega) = 3\hbar\hat{\mathbf{e}}_z$; (f) $N = 5$, $\beta_n(\omega) = 1$ for $n \in (-1, \ldots, 3)$, and $\boldsymbol{\mathcal{L}}(\omega) = 3\hbar\hat{\mathbf{e}}_z$; (g) $N = 9$, $\beta_n(\omega) = 1$ for $n \in (-3, \ldots, 5)$, and $\boldsymbol{\mathcal{L}}(\omega) = 3\hbar\hat{\mathbf{e}}_z$; (h) $N = 15$, $\beta_n(\omega) = 1$ for $n \in (-6, \ldots, 8)$, and $\boldsymbol{\mathcal{L}}(\omega) = 3\hbar\hat{\mathbf{e}}_z$. Note that the excitation light angular momentum is fixed to $m = 2$, and the excitation ring radius is $a = l_{\mathrm{SPP}}(\lambda)$. The blue lines and the red and green ellipses in the figure panels correspond to linear polarization and to right and left elliptical polarizations, respectively. Empirical data are used for gold [53].

the polarization distributions of highly coherent SPPV fields, which are composed of only a few coherent modes, to be rather intricate. As the number of modes increases, thereby reducing the field coherence, the in-plane polarization turns progressively more radial, becoming strictly radial in the limit of an infinite number of modes.

IX. CONCLUSIONS

We have introduced a class of structured partially coherent SPP fields carrying optical vortices by superposing SPPs of prescribed phase differences and arbitrary correlations at a metal-air interface. We have determined analytically the electric and magnetic coherence matrices, global degree of coherence, energy densities and flows, angular momenta, and polarization states of such SPPV fields with the help of an appropriate coherent mode representation. We have shown that the SPPV fields can carry both OAM and SAM which can be controlled by adjusting the individual SPP correlations. Whenever the individual SPPs are totally uncorrelated, the average OAM and SAM for the SPPV field are zero, and the energy flow and polarization state will both exhibit radial distribution patterns. The SPPV fields carrying OAM exhibit a circular energy flow around the excitation ring center, the signature of an optical vortex. Further, their in-plane polarization distribution has a rather intricate local structure, exhibiting nonuniform regions of circular polarization. Thus, such SPPV fields carry a nonzero average SAM. The discovered SPPV fields are expected to find numerous applications, for instance, to nanoparticle trapping [56] and angular momentum controlled SPP lasers [57].

Ultimately, our results showcase optical coherence as a flexible degree of freedom that could be harnessed to efficiently control the salient physical properties of the SPPV fields inside (and also outside [58]) the excitation ring, making these tunable vortex-carrying SPPs desirable for various applications, ranging from the enhancing the spin Hall effect of light [59] and mediating optical spin-orbit coupling [45] to manipulating optical forces in nanoplasmonic environments [56].

ACKNOWLEDGMENTS

This research was supported by the Natural Sciences and Engineering Research Council (NSERC) of Canada (Grant No. RGPIN-2018-05497), the Academy of Finland (Grants No. 310511 and No. 321066), the National Natural Sciences Foundation of China (NSFC) (Grants No. 11904247), the Natural Sciences Foundation of the Jiangsu Higher Education Institutions of China (Grant No. 19KJB140017), and the Natural Sciences Foundation of Shandong Province (Grant No. ZR2019QA004). A.N. acknowledges the Swedish Cultural Foundation in Finland for funding. S.A.P. thanks the Joensuu University Foundation.

APPENDIX A: DERIVATION OF Eqs. (20) AND (21)

Substituting the scalar coherent-mode representation of the angular SPP correlation function $W(\theta_1, \theta_2, \omega)$ of Eq. (15) into Eqs. (12) and (13), the electric and magnetic coherence matrices of the SPPV field take on the forms

$$\mathbf{W}^{(\mathrm{E})}(\mathbf{r}_1, \mathbf{r}_2, \omega) = \sum_{n=-\infty}^{\infty} \beta_n(\omega) I_{\mathrm{SPP}}(\omega) e^{-2k_\parallel''(\omega)a} \times \left[\int_0^{2\pi} e^{i(m+n)\theta_1} \hat{\mathbf{p}}(\theta_1, \omega) e^{i\mathbf{k}(\theta_1,\omega)\cdot\mathbf{r}_1} d\theta_1\right]^* \times \left[\int_0^{2\pi} e^{i(m+n)\theta_2} \hat{\mathbf{p}}(\theta_2, \omega) e^{i\mathbf{k}(\theta_2,\omega)\cdot\mathbf{r}_2} d\theta_2\right]^{\mathrm{T}}, \tag{A1}$$

$$\mathbf{W}^{(\mathrm{H})}(\mathbf{r}_1,\mathbf{r}_2,\omega) = \sum_{n=-\infty}^{\infty} \beta_n(\omega) I_{\mathrm{SPP}}(\omega) \frac{k_0^2(\omega)}{Z_0^2 |\mathbf{k}(\omega)|^2} e^{-2k_\parallel''(\omega)a} \times \left[\int_0^{2\pi} e^{i(m+n)\theta_1} \hat{\mathbf{s}}(\theta_1) e^{i\mathbf{k}(\theta_1,\omega)\cdot\mathbf{r}_1} d\theta_1\right]^* \times \left[\int_0^{2\pi} e^{i(m+n)\theta_2} \hat{\mathbf{s}}(\theta_2) e^{i\mathbf{k}(\theta_2,\omega)\cdot\mathbf{r}_2} d\theta_2\right]^{\mathrm{T}}. \tag{A2}$$

Using the wave vector of Eq. (2) and the unit polarization vectors $\hat{\mathbf{p}}(\theta, \omega)$ and $\hat{\mathbf{s}}(\theta)$ in Eqs. (A1) and (A2), we obtain the integration terms

$$\int_0^{2\pi} e^{i(m+n)\theta} \hat{\mathbf{p}}(\theta, \omega) e^{i\mathbf{k}(\theta,\omega)\cdot\mathbf{r}} d\theta = |\mathbf{k}(\omega)|^{-1} e^{ik_z(\omega)z} \int_0^{2\pi} e^{i(m+n)\theta} \times [-k_z(\omega)\cos\theta\hat{\mathbf{e}}_x - k_z(\omega)\sin\theta\hat{\mathbf{e}}_y + k_\parallel(\omega)\hat{\mathbf{e}}_z] \times e^{ik_\parallel(\omega)(x\cos\theta + y\sin\theta)} d\theta, \tag{A3}$$

$$\int_0^{2\pi} e^{i(m+n)\theta} \hat{\mathbf{s}}(\theta) e^{i\mathbf{k}(\theta,\omega)\cdot\mathbf{r}} d\theta = e^{ik_z(\omega)z} \int_0^{2\pi} e^{i(m+n)\theta} (-\sin\theta\hat{\mathbf{e}}_x + \cos\theta\hat{\mathbf{e}}_y) \times e^{ik_\parallel(\omega)(x\cos\theta + y\sin\theta)} d\theta. \tag{A4}$$

To do the integrations of each component in Eqs. (A3) and (A4), the following equations are used:

$$\int_0^{2\pi} e^{iv\theta} e^{ik_\parallel(\omega)(x\cos\theta + y\sin\theta)} d\theta = 2\pi i^v e^{iv\varphi} \mathrm{J}_v[k_\parallel(\omega)\rho], \tag{A5}$$

$$\int_0^{2\pi} e^{iv\theta} \cos\theta e^{ik_\parallel(\omega)(x\cos\theta + y\sin\theta)} d\theta = 2\pi i^v e^{iv\varphi} \frac{ie^{i\varphi}\mathrm{J}_{v+1}[k_\parallel(\omega)\rho] - ie^{-i\varphi}\mathrm{J}_{v-1}[k_\parallel(\omega)\rho]}{2}, \tag{A6}$$

$$\int_0^{2\pi} e^{iv\theta} \sin\theta e^{ik_\parallel(\omega)(x\cos\theta + y\sin\theta)} d\theta = 2\pi i^v e^{iv\varphi} \frac{ie^{i\varphi}\mathrm{J}_{v+1}[k_\parallel(\omega)\rho] + ie^{-i\varphi}\mathrm{J}_{v-1}[k_\parallel(\omega)\rho]}{2i}, \tag{A7}$$

where (ρ, φ) are cylindrical polar coordinates and $\mathrm{J}_v(\cdot)$ is a Bessel function of the first kind and of order v. Thus the x, y, and z components of Eq. (A3) read as

$$t_x^{(\mathrm{E})} = \pi |\mathbf{k}(\omega)|^{-1} e^{ik_z(\omega)z} i^{(m+n)} e^{i(m+n)\varphi} [-k_z(\omega)] \times \{ie^{i\varphi}\mathrm{J}_{m+n+1}[k_\parallel(\omega)\rho] - ie^{-i\varphi}\mathrm{J}_{m+n-1}[k_\parallel(\omega)\rho]\}, \tag{A8}$$

$$t_y^{(\mathrm{E})} = \pi |\mathbf{k}(\omega)|^{-1} e^{ik_z(\omega)z} i^{(m+n)} e^{i(m+n)\varphi} [-k_z(\omega)] \times \{e^{i\varphi}\mathrm{J}_{m+n+1}[k_\parallel(\omega)\rho] + e^{-i\varphi}\mathrm{J}_{m+n-1}[k_\parallel(\omega)\rho]\}, \tag{A9}$$

$$t_z^{(\mathrm{E})} = \pi |\mathbf{k}(\omega)|^{-1} e^{ik_z(\omega)z} i^{(m+n)} e^{i(m+n)\varphi} 2k_\parallel(\omega) \times \mathrm{J}_{m+n}[k_\parallel(\omega)\rho]. \tag{A10}$$

The x and y components of Eq. (A4) become

$$t_x^{(\mathrm{H})} = -\pi e^{ik_z(\omega)z} i^{(m+n)} e^{i(m+n)\varphi} \times \{e^{i\varphi}\mathrm{J}_{m+n+1}[k_\parallel(\omega)\rho] + e^{-i\varphi}\mathrm{J}_{m+n-1}[k_\parallel(\omega)\rho]\}, \tag{A11}$$

$$t_y^{(\mathrm{H})} = \pi e^{ik_z(\omega)z} i^{(m+n)} e^{i(m+n)\varphi} \times \{e^{i\varphi}\mathrm{J}_{m+n+1}[k_\parallel(\omega)\rho] - e^{-i\varphi}\mathrm{J}_{m+n-1}[k_\parallel(\omega)\rho]\}. \tag{A12}$$

In cylindrical coordinates, the ρ and φ components of Eqs. (A3) and (A4) are then obtained from

$$t_\rho^{(\S)} = \cos\varphi t_x^{(\S)} + \sin\varphi t_y^{(\S)}, \tag{A13}$$

$$t_\varphi^{(\S)} = -\sin\varphi t_x^{(\S)} + \cos\varphi t_y^{(\S)}, \tag{A14}$$

where $\S \in (\mathrm{E}, \mathrm{H})$ denotes the electric or magnetic component.

Substituting Eqs. (A8) and (A9), as well as Eqs. (A11) and (A12), into Eqs. (A13) and (A14), we obtain

$$t_\rho^{(\mathrm{E})} = \pi |\mathbf{k}(\omega)|^{-1} e^{ik_z(\omega)z} i^{(m+n)} e^{i(m+n)\varphi} [-ik_z(\omega)] \times \{\mathrm{J}_{m+n+1}[k_\parallel(\omega)\rho] - \mathrm{J}_{m+n-1}[k_\parallel(\omega)\rho]\}, \tag{A15}$$

$$t_\varphi^{(\mathrm{E})} = \pi |\mathbf{k}(\omega)|^{-1} e^{ik_z(\omega)z} i^{(m+n)} e^{i(m+n)\varphi} [-k_z(\omega)] \times \{\mathrm{J}_{m+n+1}[k_\parallel(\omega)\rho] + \mathrm{J}_{m+n-1}[k_\parallel(\omega)\rho]\}, \tag{A16}$$

and

$$t_\rho^{(\mathrm{H})} = -\pi e^{ik_z(\omega)z} i^{(m+n)} e^{i(m+n)\varphi} \times \{\mathrm{J}_{m+n+1}[k_\parallel(\omega)\rho] + \mathrm{J}_{m+n-1}[k_\parallel(\omega)\rho]\}, \tag{A17}$$

$$t_\varphi^{(\mathrm{H})} = i\pi e^{ik_z(\omega)z} i^{(m+n)} e^{i(m+n)\varphi} \times \{\mathrm{J}_{m+n+1}[k_\parallel(\omega)\rho] - \mathrm{J}_{m+n-1}[k_\parallel(\omega)\rho]\}. \tag{A18}$$

Inserting Eqs. (A15), (A16), and (A10) into Eq. (A1), and rearranging it in the form of the vectorial coherent mode representation in Eq. (16), we find the electric unnormalized vector coherent modes in cylindrical coordinates expressed by Eq. (20) and the corresponding modal weights given by Eq. (18). Closed forms of the magnetic unnormalized vector coherent modes in cylindrical coordinates, Eq. (21), are obtained in a similar way.

APPENDIX B: DERIVATION OF Eq. (39)

In the expression of the orbital linear momentum of the SPPV field, Eq. (32), we have

$$\mathbf{\Phi}_n^{(\S)*}(\mathbf{r},\omega)\cdot[\nabla]\mathbf{\Phi}_n^{(\S)}(\mathbf{r},\omega) = \frac{\mathbf{\Psi}_n^{(\S)*}(\mathbf{r},\omega)\cdot[\nabla]\mathbf{\Psi}_n^{(\S)}(\mathbf{r},\omega)}{\mathcal{N}_n^{(\S)2}(\omega)}, \tag{B1}$$

where $\S \in (\mathrm{E},\mathrm{H})$ denotes, as before, the electric or magnetic components. In cylindrical coordinates,

$$\mathbf{\Psi}_n^{(\S)*}(\mathbf{r},\omega)\cdot[\nabla]\mathbf{\Psi}_n^{(\S)}(\mathbf{r},\omega) = a_n^{(\S)}\hat{\mathbf{e}}_\rho + b_n^{(\S)}\hat{\mathbf{e}}_\varphi + c_n^{(\S)}\hat{\mathbf{e}}_z, \tag{B2}$$

with

$$a_n^{(\S)} = \frac{\left[\Psi_n^{(\S)}\right]_\rho^*\partial\left[\Psi_n^{(\S)}\right]_\rho + \left[\Psi_n^{(\S)}\right]_\varphi^*\partial\left[\Psi_n^{(\S)}\right]_\varphi + \left[\Psi_n^{(\S)}\right]_z^*\partial\left[\Psi_n^{(\S)}\right]_z}{\partial\rho}, \tag{B3}$$

$$b_n^{(\S)} = \frac{\left[\Psi_n^{(\S)}\right]_\rho^*\partial\left[\Psi_n^{(\S)}\right]_\rho + \left[\Psi_n^{(\S)}\right]_\varphi^*\partial\left[\Psi_n^{(\S)}\right]_\varphi + \left[\Psi_n^{(\S)}\right]_z^*\partial\left[\Psi_n^{(\S)}\right]_z}{\rho\partial\varphi}, \tag{B4}$$

$$c_n^{(\S)} = \frac{\left[\Psi_n^{(\S)}\right]_\rho^*\partial\left[\Psi_n^{(\S)}\right]_\rho + \left[\Psi_n^{(\S)}\right]_\varphi^*\partial\left[\Psi_n^{(\S)}\right]_\varphi + \left[\Psi_n^{(\S)}\right]_z^*\partial\left[\Psi_n^{(\S)}\right]_z}{\partial z}, \tag{B5}$$

where $[\Psi_n^{(\S)}]_\rho$, $[\Psi_n^{(\S)}]_\varphi$, and $[\Psi_n^{(\S)}]_z$ are the three orthogonal components of $\mathbf{\Psi}_n^{(\S)}(\mathbf{r},\omega)$ in the cylindrical coordinate system, as given in Eqs. (20) and (21). Following lengthy calculations the orbital linear momentum of the SPPV field, Eq. (32), can be written as

$$\langle\mathbf{p}(\mathbf{r},\omega)\rangle = a(\rho,z,\omega)\hat{\mathbf{e}}_\rho + b(\rho,z,\omega)\hat{\mathbf{e}}_\varphi + c(\rho,z,\omega)\hat{\mathbf{e}}_z, \tag{B6}$$

where the key point is that none of the three unit-vector coefficients depends on the azimuth angle φ. On substituting Eq. (B6) into Eq. (31), we then find

$$\langle\mathbf{l}(\mathbf{r},\omega)\rangle = \rho b(\rho,z,\omega)\hat{\mathbf{e}}_z - zb(\rho,z,\omega)\hat{\mathbf{e}}_\rho + [za(\rho,z,\omega) - \rho c(\rho,z,\omega)]\hat{\mathbf{e}}_\varphi. \tag{B7}$$

Replacing the unit vectors in cylindrical coordinates with those in Cartesian coordinates, Eq. (B7) becomes

$$\begin{aligned}\langle\mathbf{l}(\mathbf{r},\omega)\rangle = {}& \rho b(\rho,z,\omega)\hat{\mathbf{e}}_z - \{zb(\rho,z,\omega)\cos\varphi \\ & - [\rho c(\rho,z,\omega) - za(\rho,z,\omega)]\sin\varphi\}\hat{\mathbf{e}}_x \\ & - \{zb(\rho,z,\omega)\sin\varphi \\ & + [\rho c(\rho,z,\omega) - za(\rho,z,\omega)]\cos\varphi\}\hat{\mathbf{e}}_y.\end{aligned} \tag{B8}$$

To obtain the total OAM, we do a volume integration of the OAM density within the SPP excitation region. For the excitation of the SPPV field, φ ranges from 0 to 2π. Since $\int_0^{2\pi}\sin\varphi d\varphi = \int_0^{2\pi}\cos\varphi d\varphi = 0$, the x and y components of $\langle\mathbf{l}(\mathbf{r},\omega)\rangle$ vanish in the volume integration. Thus, using the explicit form of $b(\rho,z,\omega)$ (not given), we obtain the total OAM of the SPPV field as

$$\langle\mathbf{L}(\omega)\rangle = \int_{\mathrm{V}}\rho b(\rho,z,\omega)d^3\mathbf{r}\hat{\mathbf{e}}_z = \frac{1}{\omega}\sum_{n=-\infty}^{\infty}(m+n)\xi_n(\omega)\hat{\mathbf{e}}_z. \tag{B9}$$

In addition, in view of Eq. (24), the total number of photons within the SPPV field is

$$N_{\mathrm{ph}} = \mathcal{W}(\omega)/(\hbar\omega) = \sum_{n=-\infty}^{\infty}\xi_n(\omega)/(\hbar\omega). \tag{B10}$$

Finally, Eqs. (B9), (B10), and (34) yield

$$\boldsymbol{\mathcal{L}}(\omega) = \frac{\sum_{n=-\infty}^{\infty}(m+n)\xi_n(\omega)}{\sum_{n=-\infty}^{\infty}\xi_n(\omega)}\hbar\hat{\mathbf{e}}_z, \tag{B11}$$

which is Eq. (39) in the main text.

For the particular case considered in point (iii) of Sec. VI, the condition $\xi_n(\omega) = \xi_{2p-n-2m}(\omega)$ implies that $\xi_n(\omega)$ have symmetrically equal values centered at index $p-m$. Thus,

$$\sum_{n=-\infty}^{\infty}(m+n)\xi_n(\omega) = p\left[\xi_{p-m}(\omega) + 2\sum_{n'=1}^{\infty}\xi_{p-m+n'}(\omega)\right], \tag{B12}$$

$$\sum_{n=-\infty}^{\infty}\xi_n(\omega) = \left[\xi_{p-m}(\omega) + 2\sum_{n'=1}^{\infty}\xi_{p-m+n'}(\omega)\right]. \tag{B13}$$

Therefore, we obtain $\boldsymbol{\mathcal{L}}(\omega) = p\hbar\hat{\mathbf{e}}_z$.

APPENDIX C: INCOHERENT SPPV FIELDS

Bessel functions of the first kind satisfy the property

$$\mathrm{J}_{-n}(\nu) = (-1)^n\mathrm{J}_n(\nu). \tag{C1}$$

Substituting Eq. (C1) into Eqs. (20) and (21), we obtain the relations

$$\mathbf{\Psi}_n^{(\mathrm{E})\mathrm{T}}(\mathbf{r},\omega)\mathbf{\Psi}_n^{(\mathrm{E})*}(\mathbf{r},\omega) = \mathbf{\Psi}_{-n-2m}^{(\mathrm{E})\mathrm{T}}(\mathbf{r},\omega)\mathbf{\Psi}_{-n-2m}^{(\mathrm{E})*}(\mathbf{r},\omega), \tag{C2}$$

$$\mathbf{\Psi}_n^{(\mathrm{H})\mathrm{T}}(\mathbf{r},\omega)\mathbf{\Psi}_n^{(\mathrm{H})*}(\mathbf{r},\omega) = \mathbf{\Psi}_{-n-2m}^{(\mathrm{H})\mathrm{T}}(\mathbf{r},\omega)\mathbf{\Psi}_{-n-2m}^{(\mathrm{H})*}(\mathbf{r},\omega). \tag{C3}$$

Thus, the normalization factors for the unnormalized vector coherent modes have the relations $\mathcal{N}_n^{(\mathrm{E})}(\omega) = \mathcal{N}_{-n-2m}^{(\mathrm{E})}(\omega)$ and $\mathcal{N}_n^{(\mathrm{H})}(\omega) = \mathcal{N}_{-n-2m}^{(\mathrm{H})}(\omega)$. In addition, the modal weights $\{\beta_n\omega\}$ in the SPPV coherent mode representation are all equal to unity for the incoherent SPPV field. Therefore, from Eq. (18), we obtain

$$\xi_n^{(\mathrm{E})}(\omega) = \xi_{-n-2m}^{(\mathrm{E})}(\omega), \tag{C4}$$

$$\xi_n^{(\mathrm{H})}(\omega) = \xi_{-n-2m}^{(\mathrm{H})}(\omega), \tag{C5}$$

whereby the relation $\xi_n(\omega) = \xi_{-n-2m}(\omega)$ holds for the incoherent SPPV fields. The average OAM for such fields obtained from Eq. (39) thus reads

$$\boldsymbol{\mathcal{L}}(\omega) = 0. \tag{C6}$$

APPENDIX D: TIME-AVERAGED POYNTING VECTOR

Substituting Eqs. (8) and (9) into Eq. (43), we obtain for the time-averaged Poynting vector associated with the partially coherent SPPV field

$$\begin{aligned}\langle \mathbf{P}(\mathbf{r},\omega)\rangle &= \frac{1}{2}\mathrm{Re}\big\langle \mathbf{E}(\mathbf{r},\omega)\times\mathbf{H}^*(\mathbf{r},\omega)\big\rangle \\ &= \frac{-k_0(\omega)}{2Z_0|\mathbf{k}(\omega)|}\mathrm{Re}\int_0^{2\pi}\int_0^{2\pi} W(\theta_1,\theta_2,\omega)[\hat{\mathbf{p}}(\theta_2,\omega)\times\hat{\mathbf{s}}(\theta_1)] \\ &\quad\times e^{-2k_\parallel''(\omega)a}e^{i[\mathbf{k}(\theta_2,\omega)\cdot\mathbf{r}-\mathbf{k}^*(\theta_1,\omega)\cdot\mathbf{r}]}e^{im(\theta_2-\theta_1)}d\theta_1 d\theta_2, \end{aligned} \tag{D1}$$

where

$$\begin{aligned}\frac{\hat{\mathbf{p}}(\theta_2,\omega)\times\hat{\mathbf{s}}(\theta_1)}{|\mathbf{k}(\omega)|^{-1}} &= -k_\parallel(\omega)\cos\theta_1\hat{\mathbf{e}}_x - k_\parallel(\omega)\sin\theta_1\hat{\mathbf{e}}_y \\ &\quad - k_z(\omega)(\cos\theta_1\cos\theta_2+\sin\theta_1\sin\theta_2)\hat{\mathbf{e}}_z. \end{aligned} \tag{D2}$$

Making use of Eqs. (15) and (D2) in Eq. (D1), we find

$$\begin{aligned}\langle \mathbf{P}(\mathbf{r},\omega)\rangle &= \frac{k_0(\omega)S(z,\omega)}{8\pi^2 Z_0|\mathbf{k}(\omega)|^2}\mathrm{Re}\sum_{n=-\infty}^{\infty}\beta_n(\omega) \\ &\quad\times\{k_\parallel(\omega)[F_1(\mathbf{r},\omega)F_2^*(\mathbf{r},\omega)\hat{\mathbf{e}}_x + F_1(\mathbf{r},\omega)F_3^*(\mathbf{r},\omega)\hat{\mathbf{e}}_y]. \\ &\quad + k_z(\omega)[|F_2(\mathbf{r},\omega)|^2+|F_3(\mathbf{r},\omega)|^2]\hat{\mathbf{e}}_z\}, \end{aligned} \tag{D3}$$

where

$$F_1(\mathbf{r},\omega) = \int_0^{2\pi} e^{i(m+n)\theta}e^{ik_\parallel(\omega)(x\cos\theta+y\sin\theta)}d\theta, \tag{D4}$$

$$F_2(\mathbf{r},\omega) = \int_0^{2\pi} e^{i(m+n)\theta}\cos\theta\, e^{ik_\parallel(\omega)(x\cos\theta+y\sin\theta)}d\theta, \tag{D5}$$

$$F_3(\mathbf{r},\omega) = \int_0^{2\pi} e^{i(m+n)\theta}\sin\theta\, e^{ik_\parallel(\omega)(x\cos\theta+y\sin\theta)}d\theta. \tag{D6}$$

Equations (D4)–(D6) can be obtained from Eqs. (A5)–(A7). Thus, the time-averaged Poynting vector is

$$\begin{aligned}\langle \mathbf{P}(\mathbf{r},\omega)\rangle &= \frac{k_0(\omega)S(z,\omega)}{4Z_0|\mathbf{k}(\omega)|^2}\mathrm{Re}[\mathcal{P}_x(\rho,\omega)\hat{\mathbf{e}}_x \\ &\quad + \mathcal{P}_y(\rho,\omega)\hat{\mathbf{e}}_y + \mathcal{P}_z(\rho,\omega)\hat{\mathbf{e}}_z], \end{aligned} \tag{D7}$$

where the Cartesian components read

$$\begin{aligned}\mathcal{P}_x(\rho,\omega) &= ik_\parallel(\omega)\sum_{n=-\infty}^{\infty}\beta_n(\omega)\mathrm{J}_{m+n}[k_\parallel(\omega)\rho] \\ &\quad\times\{e^{i\varphi}\mathrm{J}_{m+n-1}^*[k_\parallel(\omega)\rho] - e^{-i\varphi}\mathrm{J}_{m+n+1}^*[k_\parallel(\omega)\rho]\}, \end{aligned} \tag{D8}$$

$$\begin{aligned}\mathcal{P}_y(\rho,\omega) &= k_\parallel(\omega)\sum_{n=-\infty}^{\infty}\beta_n(\omega)\mathrm{J}_{m+n}[k_\parallel(\omega)\rho] \\ &\quad\times\{e^{i\varphi}\mathrm{J}_{m+n-1}^*[k_\parallel(\omega)\rho] + e^{-i\varphi}\mathrm{J}_{m+n+1}^*[k_\parallel(\omega)\rho]\}, \end{aligned} \tag{D9}$$

$$\begin{aligned}\mathcal{P}_z(\rho,\omega) &= k_z(\omega)\sum_{n=-\infty}^{\infty}\beta_n(\omega) \\ &\quad\times\{|\mathrm{J}_{m+n-1}[k_\parallel(\omega)\rho]|^2 + |\mathrm{J}_{m+n+1}[k_\parallel(\omega)\rho]|^2\}. \end{aligned} \tag{D10}$$

In cylindrical coordinates,

$$\begin{aligned}\langle \mathbf{P}(\mathbf{r},\omega)\rangle &= \frac{k_0(\omega)S(z,\omega)}{4Z_0|\mathbf{k}(\omega)|^2}\mathrm{Re}[\mathcal{P}_\rho(\rho,\omega)\hat{\mathbf{e}}_\rho \\ &\quad + \mathcal{P}_\varphi(\rho,\omega)\hat{\mathbf{e}}_\varphi + \mathcal{P}_z(\rho,\omega)\hat{\mathbf{e}}_z], \end{aligned} \tag{D11}$$

where the ρ and φ components read

$$\begin{aligned}\mathcal{P}_\rho(\rho,\omega) &= ik_\parallel(\omega)\sum_{n=-\infty}^{\infty}\beta_n(\omega)\mathrm{J}_{m+n}[k_\parallel(\omega)\rho] \\ &\quad\times\{\mathrm{J}_{m+n-1}^*[k_\parallel(\omega)\rho] - \mathrm{J}_{m+n+1}^*[k_\parallel(\omega)\rho]\}, \end{aligned} \tag{D12}$$

$$\begin{aligned}\mathcal{P}_\varphi(\rho,\omega) &= k_\parallel(\omega)\sum_{n=-\infty}^{\infty}\beta_n(\omega)\mathrm{J}_{m+n}[k_\parallel(\omega)\rho] \\ &\quad\times\{\mathrm{J}_{m+n-1}^*[k_\parallel(\omega)\rho] + \mathrm{J}_{m+n+1}^*[k_\parallel(\omega)\rho]\}. \end{aligned} \tag{D13}$$

Making use of the following Bessel function property

$$\mathrm{J}_{\nu-1}(x) + \mathrm{J}_{\nu+1}(x) = \frac{2\nu}{x}\mathrm{J}_\nu(x), \tag{D14}$$

Eq. (D13) reduces to

$$\begin{aligned}\mathcal{P}_\varphi(\rho,\omega) &= \frac{1}{\rho}\frac{2k_\parallel(\omega)}{k_\parallel^*(\omega)}\sum_{n=-\infty}^{\infty}\beta_n(\omega) \\ &\quad\times(m+n)|\mathrm{J}_{m+n}[k_\parallel(\omega)\rho]|^2. \end{aligned} \tag{D15}$$

Equations (D11), (D12), (D15), and (D10) are, respectively, Eqs. (44)–(47) of the main text.

[1] L. M. Pismen, *Vortices in Nonlinear Fields: From Liquid Crystals to Superfluids, From Non-Equilibrium Patterns to Cosmic Strings* (Clarendon, Oxford, UK, 1999).

[2] J. F. Nye, *Natural Focusing and the Structure of Light* (Institute of Physics Publishing, Bristol, UK, 1999).

[3] L. Allen, M. W. Beijersbergen, R. J. C. Spreeuw, and J. P. Woerdman, Orbital angular momentum of light and the transformation of Laguerre-Gaussian laser modes, Phys. Rev. A **45**, 8185 (1992).

[4] M. J. Padgett, Orbital angular momentum 25 years on, Opt. Express **25**, 11265 (2017).

[5] F. Gori, M. Santarsiero, R. Borghi, and S. Vicalvi, Partially coherent sources with helicoidal modes, J. Mod. Opt. **45**, 539 (1998).

[6] S. A. Ponomarenko, A class of partially coherent beams carrying optical vortices, J. Opt. Soc. Am. A **18**, 150 (2001).

[7] G. V. Bogatyryova, C. V. Fel'de, P. V. Polyanskii, S. A. Ponomarenko, M. S. Soskin, and E. Wolf, Partially

coherent vortex beams with a separable phase, Opt. Lett. **28**, 878 (2003).
[8] C. S. D. Stahl and G. Gbur, Partially coherent vortex beams of arbitrary order, J. Opt. Soc. Am. A **34**, 1793 (2017).
[9] X. Chen, J. Li, S. M. H. Rafsanjani, and O. Korotkova, Opt. Lett. **43**, 3590 (2018).
[10] D. M. Palacios, I. D. Maleev, A. S. Marathay, and G. A. Swartzlander, Spatial Correlation Singularity of a Vortex Field, Phys. Rev. Lett. **92**, 143905 (2004).
[11] W. Wang, Z. Duan, S. G. Hanson, Y. Miyamoto, and M. Takeda, Experimental Study of Coherence Vortices: Local Properties of Phase Singularities in a Spatial Coherence Function, Phys. Rev. Lett. **96**, 073902 (2006).
[12] T. van Dijk and T. D. Visser, Evolution of singularities in a partially coherent vortex beam, J. Opt. Soc. Am. A **26**, 741 (2009).
[13] W. Wang and M. Takeda, Coherence Current, Coherence Vortex, and the Conservation Law of Coherence, Phys. Rev. Lett. **96**, 223904 (2006).
[14] B. Redding, M. A. Choma, and H. Cao, Speckle-free laser imaging using random laser illumination, Nat. Photonics **6**, 355 (2012).
[15] A. Gatti, E. Brambilla, M. Bache, and L. A. Lugiato, Ghost Imaging with Thermal Light: Comparing Entanglement and Classical Correlation, Phys. Rev. Lett. **93**, 093602 (2004).
[16] T. Shirai, A. Dogariu, and E. Wolf, Mode analysis of spreading of partially coherent beams propagating through atmospheric turbulence, J. Opt. Soc. Am. A **20**, 1094 (2003).
[17] X. Liu, J. Yu, Y. Chen, Y. Cai, and S. A. Ponomarenko, Propagation of optical coherence lattices in the turbulent atmosphere, Opt. Lett. **41**, 4182 (2016).
[18] J. M. Auñón and M. Nieto-Vesperinas, Partially coherent fluctuating sources that produce the same optical force as a laser beam, Opt. Lett. **38**, 2869 (2013).
[19] C. C. Jeng, M. F. Shih, K. Motzek, and Y. Kivshar, Partially Incoherent Optical Vortices in Self-Focusing Nonlinear Media, Phys. Rev. Lett. **92**, 043904 (2004).
[20] X. Liu, Y. Shen, L. Liu, F. Wang, and Y. Cai, Experimental demonstration of vortex phase-induced reduction in scintillation of a partially coherent beam, Opt. Lett. **38**, 5323 (2013).
[21] Y. Gorodetski, A. Niv, V. Kleiner, and E. Hasman, Observation of the Spin-Based Plasmonic Effect in Nanoscale Structures, Phys. Rev. Lett. **101**, 043903 (2008).
[22] V. E. Lembessis, M. Babiker, and D. L. Andrews, Surface optical vortices, Phys. Rev. A **79**, 011806(R) (2009).
[23] H. Kim, J. Park, S.-W. Cho, S.-Y. Lee, M. Kang, and B. Lee, Synthesis and dynamic switching of surface plasmon vortices with plasmonic vortex lens, Nano Lett. **10**, 529 (2010).
[24] I. Dolev, I. Epstein, and A. Arie, Surface-Plasmon Holographic Beam Shaping, Phys. Rev. Lett. **109**, 203903 (2012).
[25] I. V. Dzedolik and V. Pereskokov, Control of plasmon-polariton vortices on the surface of a metal layer, J. Opt. Soc. Am. A **35**, 1420 (2018).
[26] G. Spektor, D. Kilbane, A. K. Mahro, B. Frank, S. Ristok, L. Gal, P. Kahl, D. Podbiel, S. Mathias, H. Giessen, F.-J. Meyer zu Heringdorf, M. Orenstein, and M. Aeschlimann, Revealing the subfemtosecond dynamics of orbital angular momentum in nanoplasmonic vortices, Science **355**, 1187 (2017).
[27] H. Ren, X. Li, Q. Zhang, and M. Gu, On-chip noninterference angular momentum multiplexing of broadband light, Science **352**, 805 (2016).
[28] L. Novotny and B. Hecht, *Principles of Nano-Optics*, 2nd ed. (Cambridge University Press, Cambridge, UK, 2012).
[29] A. Norrman, T. Setälä, and A. T. Friberg, Partial coherence and polarization of a two-mode surface-plasmon polariton field at a metallic nanoslab, Opt. Express **23**, 20696 (2015).
[30] A. Norrman, S. A. Ponomarenko, and A. T. Friberg, Partially coherent surface plasmon polaritons, EPL **116**, 64001 (2016).
[31] Y. Chen, A. Norrman, S. A. Ponomarenko, and A. T. Friberg, Plasmon coherence determination by nanoscattering, Opt. Lett. **42**, 3279 (2017).
[32] H. Mao, Y. Chen, S. A. Ponomarenko, and A. T. Friberg, Coherent pseudo-mode representation of partially coherent surface plasmon polaritons, Opt. Lett. **43**, 1395 (2018).
[33] S. Daniel, K. Saastamoinen, S. A. Ponomarenko, and A. T. Friberg, Scattering of partially coherent surface plasmon polariton fields by metallic nanostripe, J. Eur. Opt. Soc.-Rapid Publ. **15**, 4 (2019).
[34] A. Bouhelier and G. P. Wiederrecht, Excitation of broadband surface plasmon polaritons: Plasmonic continuum spectroscopy, Phys. Rev. B **71**, 195406 (2005).
[35] W. Liu, D. N. Neshev, A. E. Miroshnichenko, I. V. Shadrivov, and Y. S. Kivshar, Polychromatic nanofocusing of surface plasmon polaritons, Phys. Rev. B **83**, 073404 (2011).
[36] S. Aberra Guebrou, C. Symonds, E. Homeyer, J. C. Plenet, Y. N. Gartstein, V. M. Agranovich, and J. Bellessa, Coherent Emission from a Disordered Organic Semiconductor Induced by Strong Coupling with Surface Plasmons, Phys. Rev. Lett. **108**, 066401 (2012).
[37] Y. Chen, A. Norrman, S. A. Ponomarenko, and A. T. Friberg, Partially coherent axiconic surface plasmon polariton fields, Phys. Rev. A **97**, 041801(R) (2018).
[38] Y. Chen, A. Norrman, S. A. Ponomarenko, and A. T. Friberg, Coherence lattices in surface plasmon polariton fields, Opt. Lett. **43**, 3429 (2018).
[39] P. S. Tan, X.-C. Yuan, J. Lin, Q. Wang, T. Mei, R. E. Burge, and G. G. Mu, Surface plasmon polaritons generated by optical vortex beams, Appl. Phys. Lett. **92**, 111108 (2008).
[40] P. Li, Y. Zhang, S. Liu, C. Ma, L. Han, H. Cheng, and J. Zhao, Generation of perfect vectorial vortex beams, Opt. Lett. **41**, 2205 (2016).
[41] X. Wang, Y. Zhang, Y. Dai, C. Min, and X. Yuan, Enhancing plasmonic trapping with a perfect radially polarized beam, Photonics Res. **6**, 847 (2018).
[42] S. Wei, G. Si, M. Malek, S. K. Earl, L. Du, S. S. Kou, X. Yuan, and J. Lin, Toward broadband dynamic structuring of a complex plasmonic field, Sci. Adv. **4**, eaao0533 (2018).
[43] A. Norrman, T. Setälä, and A. T. Friberg, Long-range higher-order surface-plasmon polaritons, Phys. Rev. A **90**, 053849 (2014).
[44] A. Norrman, T. Setälä, and A. T. Friberg, Surface-plasmon polariton solutions at a lossy slab in a symmetric surrounding, Opt. Express **22**, 4628 (2014).
[45] K. Y. Bliokh, F. J. Rodrguez-Fortuo, F. Nori, and A. V. Zayats, Spin-orbit interactions of light, Nat. Photonics **9**, 796 (2015).
[46] L. Mandel and E. Wolf, *Optical Coherence and Quantum Optics* (Cambridge University Press, Cambridge, UK, 1995).

[47] J. Turunen, A. Vasara, and A. T. Friberg, Propagation invariance and self-imaging in variable-coherence optics, J. Opt. Soc. Am. A **8**, 282 (1991).

[48] J. Tervo, T. Setälä, and A. T. Friberg, Theory of partially coherent electromagnetic fields in the space-frequency domain, J. Opt. Soc. Am. A **21**, 2205 (2004).

[49] K. Blomstedt, T. Setälä, and A. T. Friberg, Effective degree of coherence: general theory and application to electromagnetic fields, J. Opt. A: Pure Appl. Opt. **9**, 907 (2007).

[50] K. Y. Bliokh and F. Nori, Transverse and longitudinal angular momenta of light, Phys. Rep. **592**, 1 (2015).

[51] M. Neugebauer, T. Bauer, A. Aiello, and P. Banzer, Measuring the Transverse Spin Density of Light, Phys. Rev. Lett. **114**, 063901 (2015).

[52] M. Neugebauer, J. S. Eismann, T. Bauer, and P. Banzer, Magnetic and Electric Transverse Spin Density of Spatially Confined Light, Phys. Rev. X **8**, 021042 (2018).

[53] *Handbook of Optical Constants of Solids*, edited by E. D. Palik (Academic, Orlando, FL, 1998).

[54] T. Setälä, A. Shevchenko, M. Kaivola, and A. T. Friberg, Degree of polarization for optical near fields, Phys. Rev. E **66**, 016615 (2002).

[55] A. T. Friberg and T. Setälä, Electromagnetic theory of optical coherence (invited), J. Opt. Soc. Am. A **33**, 2431 (2016).

[56] M. I. Petrov, S. V. Sukhov, A. A. Bogdanov, A. S. Shalin, and A. Dogariu, Surface plasmon polariton assisted optical pulling force, Laser Photonics Rev. **10**, 116 (2016).

[57] P. Berini and I. De Leon, Surface plasmon-polariton amplifiers and lasers, Nat. Photonics **6**, 16 (2011).

[58] Y. Gorodetski, S. Nechayev, V. Kleiner, and E. Hasman, Plasmonic Aharonov-Bohm effect: Optical spin as the magnetic flux parameter, Phys. Rev. B **82**, 125433 (2010).

[59] X. Ling, X. Zhou, K. Huang, Y. Liu, C.-W. Qiu, H. Luo, and S. Wen, Recent advances in the spin Hall effect of light, Rep. Prog. Phys. **80**, 066401 (2017).